




Review Paper

# Recent advances in characterising irradiation damage in tungsten for fusion power



Suchandrima Das<sup>1</sup> 

Received: 26 August 2019 / Accepted: 29 October 2019 / Published online: 15 November 2019

© The Author(s) 2019 

## Abstract

Tungsten is the front-runner candidate for building the plasma-facing armour components for future fusion reactors. However, in-service irradiation by fusion-neutrons and helium will create lattice-defects in the material, compromising its properties and lifetime. Improving the component's resilience to radiation damage and accurately predicting the lifetime of irradiated components is key for commercial feasibility of the reactor. For this purpose, understanding the creation and evolution of radiation damage is essential. This paper reviews recent advances in characterising radiation damage through experimental and modelling techniques. Tungsten-ion- and helium-ion-implantation are commonly used to mimic the damage created by neutron- and helium-irradiation respectively. Defects ( $> 1.5$  nm) can be directly imaged using transmission electron microscopy while all defects (size-independent), may be indirectly probed by measuring lattice strains induced by them (using diffraction techniques; synchrotron X-rays or high-resolution electron-backscatter). Neutron-irradiation produces mainly  $\frac{1}{2}\langle 111 \rangle$  prismatic loops. Loop-interaction and structural organisation evolves with changing implantation dose and temperature. Helium-irradiation,  $< 573$  K, induces formation of small helium-vacancy clusters, which evolve into bubbles, blisters and "fuzz" structure with changing temperature and dose. Nano-indentation or micro-cantilever bending tests can be used to examine mechanical properties of ion-implanted layers. Both helium- and neutron-implantation defects induce increased hardening often followed by subsequent strain-softening and localised deformation. Such irradiation-induced alterations are detrimental to material ductility and long-term structural integrity of tungsten-based components. Development of physically-based material models that capture the physics of underlying irradiation-induced changes, inspire confidence of reliably using simulations to predict mechanical behaviour and in-service performance of irradiated engineering components in future.

**Keywords** Tungsten · Fusion neutron · Helium-implantation · Hydrogen plasma · Irradiation defects · Crystal-plasticity model of irradiation damage

## 1 Introduction

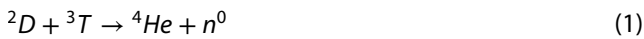
The predicted rise in global population is anticipated to increase energy consumption by 48% by 2040 [1]. Large part of the future energy needs will have to be met by non-fossil-fuel sources. Renewable sources such as wind, solar, etc. depend on varying environmental conditions and cannot guarantee constant production. Moreover, there are technological and financial difficulties in storing

the energy generated from these sources. To ensure regular supply of baseload or to meet unanticipated energy demands, foreseeable and invariant energy sources are needed. Nuclear fusion promises to be such an efficient and reliable energy source. In contrast with fission, it does not face the problems of generating long term radioactive waste, limited fuel supply and lack of public and political tolerance.

✉ Suchandrima Das, suchandrima90@gmail.com | <sup>1</sup>Department of Engineering Science, University of Oxford, Oxford OX1 3PJ, UK.



However, before fusion reactors can be in full operation and commercially viable, they still require substantial research, particularly in areas of plasma physics, and reactor materials. The largest tokamak currently in operation, the Joint European Torus (JET), has shown the successful operation of a fusion reactor with a deuterium–tritium fuel mixture [2] given by



However, JET is a small scale reactor; primarily build to study the behaviour of the plasma under fusion conditions. A new fusion energy project, the ITER, with 10 times the plasma volume of JET, is now being built [3]. The ambitious ITER project, involving several countries, targets to begin operation in 2035, and is being designed to be the first fusion reactor capable of producing net energy.

The fusion reaction (Eq. 1) releases 17.6 MeV of fusion energy, split between a high-energy neutron (14.1 MeV) and a charged  ${}^4\text{He}$  nucleus [4, 5]. The neutrons generated will be absorbed in a blanket containing lithium. Reaction between lithium and neutrons produce tritium [6], which is re-cycled as input fuel for the reactor. A coolant flowing through the blanket collects the heat energy, to produce electricity by conventional methods. Impurities created during operation, such as eroded particles from the reactor and helium (fusion reaction waste product), must be purged off, in order to sustain the fusion reaction. The divertor, located at the bottom of the vacuum vessel, removes these unwanted ions [3].

Plasma facing surface such as the blanket or the “first wall”, where the neutrons are absorbed, and the divertor, experience high heat loads. The blanket gets deposited with almost 85% of the fusion power and experience heat loads of about 2 MW/m<sup>2</sup>. The divertor too, being responsible for exhausting ~ 15% of total fusion power may experience heat load of 10–20 MW/m<sup>2</sup> [6]. To shield the structural components of the divertor and the first wall from the plasma, a protection layer or armour components are applied on these components.

The plasma-facing armour components will be exposed not only to high temperatures (> 900 °C) and high heat loads, but also bombardment by the high-energy fusion neutrons and gaseous elements like hydrogen and helium [4, 6–9]. Interaction of the neutrons with the crystal lattice generates collision cascades and defect accumulation in the material [10, 11]. Also it can cause transmutation, resulting in the formation of rhenium, osmium, tantalum, hydrogen or helium; elements which can aggravate the radiation damage by their interaction with the irradiation-induced defects [12, 13]. At the anticipated operating temperatures, interstitial mobility of gasses is high, allowing hydrogen and helium (either introduced from plasma or

formed from transmutation) to diffuse to defects, cracks or grain boundaries, causing embrittlement and hardening [14–17].

Given the extreme conditions that the plasma facing armour material has to withstand, two materials may be suitable: SiC-CFC (carbon-fibre composites) with a window of ~ 650–950 °C and tungsten with a window of 800–1300 °C [18]. Of the two, the CFC materials, have pronounced advantages in terms of high thermal conductivity (200–500 W/mK), minimal plasma contamination (12% allowable plasma concentration) and a capability to withstand cyclic thermal loading of up to 19 MW/m<sup>2</sup> [19]. However, their excellent thermal conductivity reduces to about 50 W/mK when irradiated with a low neutron fluence of 0.2 dpa [19]. Tritium is the fuel for the fusion reactor and being a radioactive element, only a certain inventory limit (~ 700 g) is permitted. It has been seen that CFC has a high tritium retention rate, wherein, the inventory limit can be reached in a few tens of plasma discharges. On the contrary, in tungsten, the inventory limit is not reached even after 18,000 plasma discharges [20].

Another disadvantage of CFC materials is their enhanced erosion due to chemical interaction with the hydrogen plasma. Investigation at plasma gun facilities has shown that a few microns can be eroded with every plasma pulse [21]. The high rate of tritium retention and erosion indicates that CFC materials may have to be frequently repaired and replaced, which makes them commercially unattractive. Comparison of erosion as induced by deuterium ions from beryllium, tungsten and carbon (Fig. 1) shows that the erosion yield from tungsten is the lowest, being almost an order of magnitude lower than that from carbon, for energy ranges between 100 and 10,000 eV [22]. Thus tungsten, with its high melting point (3422 °C), notable strength at high temperature, low tritium inventory, low sputtering rate and the ability to retain these properties after irradiation, has been chosen by ITER for building the armour components [3, 6, 23, 24].

However, challenges in use of tungsten armour components arise from tungsten's low fracture toughness, high brittle to ductile transition temperature (BDTT) and poor machinability [25]. Moreover, intense radiation in-service can lower the lifetime of the tungsten component. For a commercially viable fusion reactor the divertor armour material and the first wall component should have a lifetime of at least two and five full-power years respectively [13]. Irradiation by fusion neutrons and gaseous elements, has the potential to become life limiting for the tungsten component, with significant economic consequences for fusion power [26, 27]. To develop new strategies for improving the irradiation resistance of tungsten components, fundamental understanding of defect generation and property evolution in tungsten is urgently required.

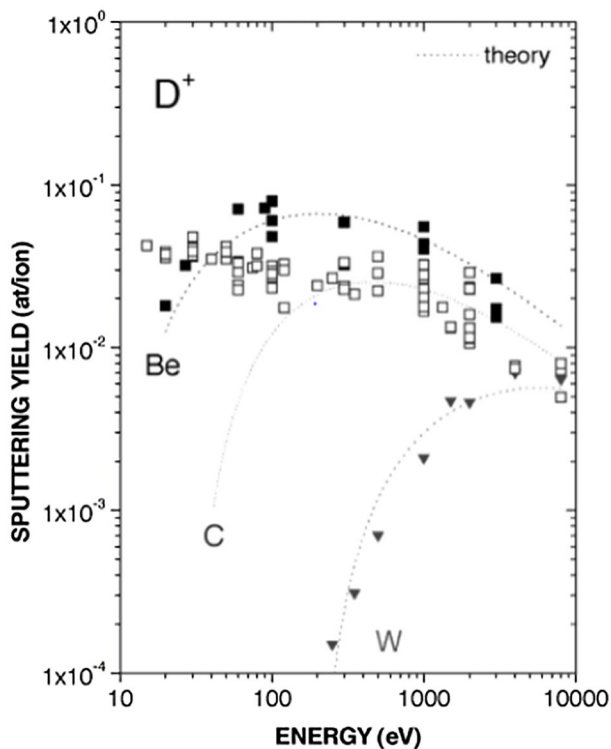


**Fig. 1** Comparison of measured values for the sputtering yield at normalised incidence for beryllium (closed squares), carbon (open squares), and tungsten (closed triangles) by deuterium ions with results from analytical modelling of physical sputtering [22]

This paper reviews the recent advances made in development of tungsten for fusion power and in characterising irradiation damage in tungsten.

## 2 Engineering properties of tungsten

The mechanical properties of pristine tungsten is discussed here to build the foundation for analysis of irradiation induced changes. Traditionally tungsten has been used as a functional material, such as in X-ray targets or in light bulb filaments, owing to its high melting temperature and its electronic structure [28]. The lack of structural use is because tungsten, by virtue of its body centred cubic (bcc) structure, exhibits brittle fracture at low temperature and ductile failure at higher temperatures. The BDTT is largely strain-rate dependent and is typically about 100–200 °C for tungsten for strain rates  $4 \times 10^{-5}$  to  $5 \times 10^{-2}$  [29]. An added disadvantage is its low fracture toughness, with polycrystalline samples having a fracture toughness below 10 MPa/m [30]. This mechanical behaviour is governed by dislocation mobility which is influenced by both intrinsic and extrinsic factors.

The intrinsic factor controlling dislocation mobility is the Peierl's stress, i.e. the minimum required shear stress (theoretically or computationally derived at 0 K) to move a dislocation from one Peierl's valley to the next [31]. The atomic bond strength, the crystal structure, the shear modulus, dislocation width, Burgers' vector and Poisson's ratio, determine the Peierl's stress [32]. Tungsten, with its non-close-packed bcc structure and strong atomic bond, has an inherently high Peierl's stress and consequently a low intrinsic dislocation mobility.

In bcc crystals, screw dislocations glide by nucleation and movement of kink pairs along the dislocation line [33, 34]. Being a thermally activated process, dislocation mobility and thus BDTT follows an Arrhenius relationship,  $T_{BDT} = \frac{E_{BDT}}{k \left( \ln \left( \frac{\dot{\epsilon}}{A} \right) \right)}$  where  $T_{BDT}$  is the brittle-to-ductile transition temperature,  $E_{BDT}$  is the corresponding activation energy,  $k$  is the Boltzmann constant,  $\dot{\epsilon}$  strain rate and  $A$  is a constant. Thus  $T_{BDT}$  depends on the strain-rate and the  $E_{BDT}$ . It has been reported that in tungsten, the activation energy for double kink formation on screw dislocations decides  $E_{BDT}$  [29]. This could be due to the rate of crystal plasticity being more strongly controlled by screw dislocations than edge, given their much lower mobility as compared to edge dislocations [35]. While  $E_{BDT}$  is about 1.05 eV for pure tungsten it is seen to increase to about 1.45 eV for impure sintered material [29]. These values of  $E_{BDT}$  suggest that the BDTT is sensitive to impurities.

Further, extrinsic factors such as processing of tungsten, can affect its purity which in turn can influence the dislocation mobility and BDTT. Interstitial impurities introduced during processing such as carbon, nitrogen or oxygen can pin both edge and screw dislocations [36].  $T_{BDT}$  in high purity deformed tungsten is found to be  $\sim 90$  K lower than in sintered deformed tungsten for all strain-rates [37]. Solute atoms like phosphorus can gather at grain boundaries and cause tungsten to become more brittle and promote inter-granular failure [30].

Thus in summary, the low mobility of dislocations in tungsten is central to its brittleness at room temperature, high BDTT, and inherently poor mechanical behaviour.

## 3 Improving tungsten's engineering properties for fusion power

Tungsten based armour components require significant development before they can be put to service. Presence of impurities and the type of thermal treatment chosen will influence the fracture behaviour [30]. Tungsten's poor ductility makes it difficult to carry out deep drawing needed to form the divertor components. Further, shattering of the brittle tungsten in the plasma facing tiles, could

result in quenching the fusion reaction, by the introduction of the heavy ions into the plasma.

DFT calculations show that addition of rhenium to tungsten may improve its ductility by changing dislocation core structure, reducing Peierl's stress, increasing the number of available slip planes and reducing the critical stress required for plasticity to set in [38]. However, irradiation-induced clustering of rhenium sets in at high damage doses and leads to substantial hardening as rhenium clusters act as efficient obstacles to dislocation motion [27, 39, 40]. Other elements such as tantalum, vanadium, molybdenum and titanium can form a solid solution with tungsten. Studies have shown however, that alloys of tungsten with the above elements result in increasing the BDTT and brittle, inter-granular failure along high angle grain boundaries are observed in such alloys [41]. Since alloying tungsten does not have much advantages, an alternative method of forming tungsten fibre reinforced tungsten composites was investigated to increase the fracture toughness. It is anticipated that this can toughen the material by controlling cracking and friction at engineered fibre/matrix interfaces and causing effective energy dissipation [42]. For instance, the bending strength of tungsten fibre reinforced tungsten/copper composites (with ~ 5.5 wt% tungsten fibres) was found to increase by 12.7% [43].

The upper limit of the operating temperature is constrained by properties of recrystallisation and creep. Often the plasmas are seeded with impurities such as nitrogen to radiate energy and lower the heat load on the divertor. If the recrystallisation temperature of tungsten is improved, concentrations of such impurities in the plasma could be reduced. ODS tungsten alloys have been considered to address this issue. However, addition of the alloying

elements and the presence of the oxide particles lowers the fracture toughness of the material. But for instance three-point bending tests in ODS tungsten, W-2%Y<sub>2</sub>O<sub>3</sub>, showed that the composite is ductile above 400 °C [44]. Also fine grained W-TiC and W-ZrC composites were found to withstand a heat flux 100% higher than pure tungsten while displaying higher tensile strength [45]. These observations inspire confidence that tungsten alloys with rare-earth oxides or carbides are promising materials for further investigation.

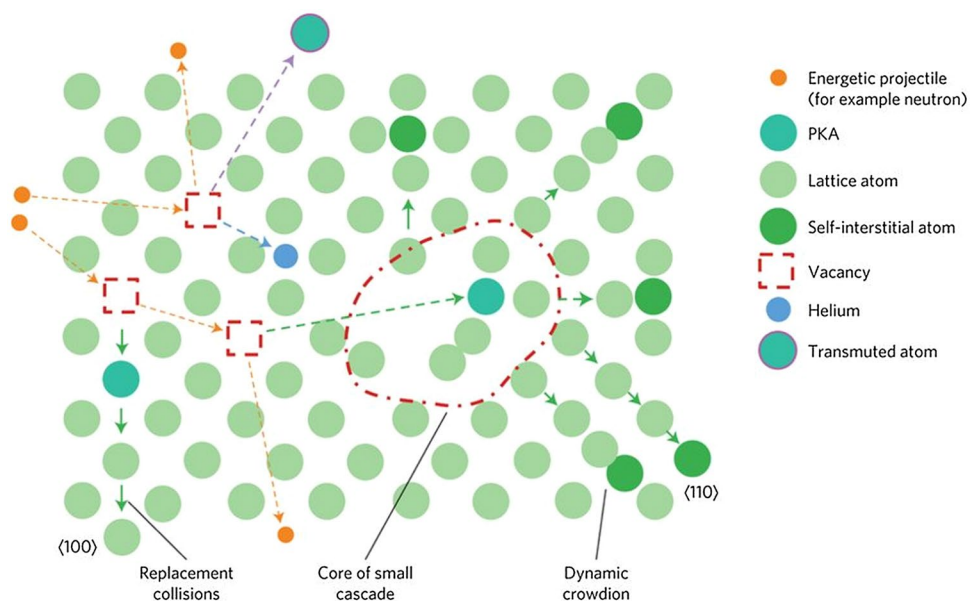
In summary, the key improvement areas for tungsten as a fusion material, are increasing ductility, formability and its fracture toughness without adversely affecting the advantageous properties of high thermal conductivity, recrystallisation and creep behaviour. To best judge the degree of improvement needed and estimate the feasibility of the current component designs, it is crucial to understand how properties may change in-service. Thus studying tungsten irradiated by neutrons, hydrogen and helium or corresponding representative models is essential for developing more resilient tungsten armour components.

## 4 Methods for studying radiation damage

### 4.1 Creation and evolution of radiation defects

As neutron and other particles bombard the material, the regular crystal lattice is disturbed. An example of the disturbed crystal lattice is shown in Fig. 2. The impacting particles knock atoms from their lattice positions, creating primary-knock-on atoms (PKAs) [26]. These then produce more lattice displacements (cascade damage) as they

**Fig. 2** Schematic illustration of irradiation damage [139]



move through the material. The vacant site created by a displaced atom is known as a vacancy defect, while the displaced atom itself, accommodated at an interstitial site is known as a self-interstitial atom (SIA). The combination of a vacancy and a SIA is known as a Frenkel Pair.

Besides point defects, dislocations are also created, where the crystallographic registry is lost along a line [35]. Dislocations are thus often described as a boundary line on the slip plane, demarcating the region where slip has occurred from the region where it has not. They significantly influence properties like hardness, ductility, toughness etc. There can be three types of dislocations; screw dislocation, where the direction of the dislocation line is parallel to the slip direction, edge dislocation where the direction of the dislocation line and the slip direction are orthogonal, and mixed dislocation where the direction of the dislocation line has one component parallel to the slip direction and one component orthogonal to it.

The interaction between defects and their eventual fate depends on the defect density and their mobility. Several reaction paths are possible: defects can be lost at grain boundaries, can be absorbed by other defect clusters, disappear due to mutual annihilation such as that of vacancy and interstitial or remain in the material [46]. The irradiation-induced defects when retained in the material, create pinning obstacles for gliding dislocations. Vacancies can accumulate to create volume defects in the form of voids [47], whose diameter can change with the dose [27]. Evolution of loops, voids and other associated phenomena such as creep or swelling depends on the reaction path adopted in the material as the microstructure evolves [46].

The number of displacements per atom created by the impacting particle i.e. the dpa, is a common measure of radiation damage. However, it must be noted that most of the atomic displacements initiated by the impacting particle, anneal out and only few remain. It was found that for helium implantation, only about 1% of the calculated dpa was retained in the material [48]. Thus, there is an element of uncertainty in using dpa as a measure of radiation damage. However, in absence of a substitute accepted convention, damage levels in this article will be reported in dpa.

## 4.2 Emulating fusion irradiation damage

To understand the combined damage caused due to irradiation by neutrons and gaseous elements, ideally tungsten exposed to the real fusion environment should be examined. As the reactor conditions cannot be recreated yet, alternative means are necessary to experimentally study irradiation damage. Fission neutron irradiation can be used to emulate fusion neutron damage [10, 49]. However there remain some concerns about dissimilarities in the energy spectrum of and damage microstructure

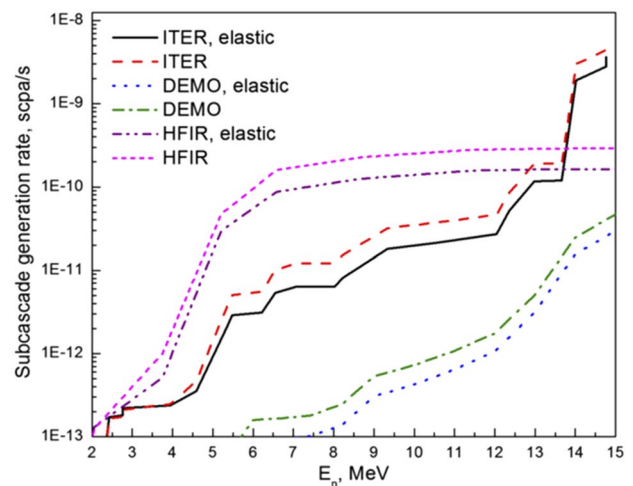


Fig. 3 Generation rates of sub-cascades for tungsten in HFIR, DEMO and ITER [54]

generated by fission and fusion neutrons. Comparison between the neutron spectra from fusion prototype reactor DEMO [50] and that from a typical fission source HFR-F8 [51] showed distinct differences, particularly beyond 5 MeV. Below 5 MeV, the HFR-8 spectrum, was seen to be aligned with the DEMO spectrum, but about five times lower than the DEMO spectrum. However, above 5 MeV, while the fusion spectrum goes up to 14 MeV, the fission spectrum was found to drop sharply, indicating the absence of high energy knock-on atoms.

The PKA energy heavily influences the cascade damage morphology [52]. Beyond a certain PKA, energy cascades can split to create sub-cascades, introducing further complexity in the microstructure. Sub-cascade generation is dependent on the radius of damage zone (R) produced by a secondary knock on atom (SKA). SKAs can be generated by two elastic collisions [53]. If the mean distance  $\lambda(E)$  between two collisions produced by PKA of energy E, is greater than R, then a sub-cascade is generated [53]. Ryazanov et al. [54] found that the sub-cascade generation rate in tungsten in HFIR, particularly for low neutron energies (< 1 keV), is two–three orders of magnitude higher than in DEMO and ITER (shown in Fig. 3). A Monte Carlo binary collision approximation model has shown that high energy cascade fragments mainly have small defect clusters, while low energy sub-cascades, produce more defects and larger defect clusters [55]. Thus, owing to its higher sub-cascade generation rate, irradiation with fission neutrons, may overestimate the damage produced by fusion neutrons.

Besides creating lattice defects, neutron irradiation can also produce gaseous element through transmutation. However, for the same neutron fluence, the amount of hydrogen and helium produced in tungsten, differs in

fission and fusion environments. For the same neutron fluence of  $10^{23}$  n/cm<sup>2</sup>, the relatively softer energy spectrum of the fission neutrons (HFIR) produced only 0.0008 appm/dpa of helium while magnetic confinement (MFE) and inertial confinement fusion (IFE) produced 0.6 and 0.5 appm/dpa of helium respectively [56]. The hydrogen produced is also underestimated by fission neutron irradiation, where HFIR produces 0.003 appm/dpa in comparison with 1.8 and 1.2 appm/dpa produced by MFE and IFE respectively.

The significant differences between the neutron spectrum from fission and fusion sources and the consequent effects on damage production has motivated the development of a relevant fusion source, where the evolution of properties of candidate materials, for the commercial fusion reactor, can be fully evaluated over the targeted component lifetime. This has led to the formation of a multinational scientific research program, the International Fusion Materials Irradiation Facility, also known as IFMIF, which aims to produce a neutron spectrum similar to that anticipated at the plasma-facing components of the fusion reactor. This is a promising source for inducing fusion relevant irradiation damage in materials for experimental characterisation. However, the main problem with neutron irradiation is that it renders the materials to be radioactive and unsuitable for regular handling and experiments in the laboratory. Further, they involve a high turn-around time, rendering the experiments to be expensive and difficult to reproduce. Also, experimental observations from such samples are unable to reveal the mechanism governing them, as it is difficult to decode the individual contribution of neutrons, helium and other elements formed through transmutation.

Ion-implantation is a cost- and time-effective means of emulating the radiation damage. Self-ion implanted and helium-implanted tungsten are commonly used as models to study neutron and helium irradiated tungsten [57, 58]. However, as limited ion-penetration depth generates only few micron thick damage layer (exact thickness depending on the implantation energy), techniques for studying the material at this scale are required. It is also important to note that the PKA energy and the displacement rate ( $10^{-3}$ – $10^{-4}$  dpa/s) from high energy ion bombardment, is higher than that for fusion neutrons (displacement rate  $10^{-7}$ – $10^{-8}$  dpa/s) implying differences in damage microstructure induced by ion-implantation and fusion neutrons [59]. Temporal overlap of cascades, caused by the higher displacement rates, are of particular concern, especially in presence of impurities like carbon, which can decelerate the long term damage evolution.

### 4.3 Techniques to study irradiated materials

The irradiated materials can be studied using a combination of experimental and modelling techniques. Transmission electron microscopy (TEM) is extensively used to image the radiation defects [10, 49, 60], their evolution with temperature, fluence [61] and the time and temperature dependence of defect recovery [62]. While TEM offers the great advantage of direct imaging of defects, it requires extensive and invasive sample preparation and cannot resolve defects smaller than 1.5 nm [63]. Another technique often adopted for examining vacancy type irradiation defects in crystalline materials like tungsten, is positron annihilation spectroscopy (PAS); for example to detect the annealing of radiation defects involving vacancy migration and evolution of vacancy dominated large defect clusters with changing temperature [64] or change in deuterium retention in tungsten due to deuterium trapping in vacancy-type defects [65] or to reliably estimate elementary point defects formed at cryogenic temperatures and their recovery kinetics as foundation for building predictive models on evolution of radiation damage [66]. However, interpretation of the PAS measurements requires supportive experimental methods or characterization techniques such as electron paramagnetic resonance (EPR). Further complexities may include distinction of vacancies from nano-voids or identification of defect combinations of vacancies and self-interstitials. Alternatively, the entire defect population (irrespective of size) can be probed by measuring the lattice strain induced by them using synchrotron X-ray micro-diffraction which uniquely permits the determination of lattice strain with sub-micron 3D spatial resolution and  $\sim 10^{-4}$  strain sensitivity [48, 58, 67–69]. Using a combination of this approach and electronic structure calculations, it is possible to deduce the nature of the defect (vacancy or self-interstitial), morphology and its depth-resolved distribution in the implanted layer [48, 70]. Electronic structure or first principle calculations provide information about the atomistic level, such as that of interaction between radiation defects and solute atoms [54, 55, 71–74]. To account for different length scales and time scales, several different complementary atomistic modelling techniques such as Density Functional Theory (DFT) calculations, Molecular Dynamics (MD), Kinetic Monte Carlo (KMC), Mean Field Rate Theory (MFRT) and Dislocation Dynamics (DD) are used [75].

Mechanical properties of thin irradiated layers obtained by ion-implantation can be characterised by techniques like micro-cantilever bending tests or nano-indentation, which involves a diamond tip being driven into the material surface whilst measuring both the applied load and displacement [76–81]. While there are

several challenges associated with nano-indentation measurements such as the indentation size effect [82] or the unaccounted for complexities of the deformation fields such as 'pile up' and sink-in around the indent [78], it is a great qualitative tool that enables probing deformation behaviour on very small scales that could not be otherwise interrogated.

Deformation-induced lattice distortions, in such thin ion-implanted layers can then be assessed using non-invasive techniques such as micro-beam Laue diffraction and high-resolution electron back scatter diffraction (HR-EBSD) [58, 83, 84]. HR-EBSD allows calculation of the residual elastic lattice strain and lattice rotation tensors ( $\sim 1 \times 10^{-4}$  rad) by cross-correlating the shift and distortion of a particular electron diffraction pattern with respect to a number of regions of interest (ROIs) from a reference pattern, within the same grain [85, 86]. While it has high spatial resolution, its sensitivity to small strains is limited and measurements are restricted to the sample surface. As such it complements very well the technique of Laue diffraction measurement which has relatively lower spatial resolution, but good sensitivity to smaller, far-field strains. In addition, Laue measurements help to probe beneath the surface by providing a 3D measurement of the deformation field in a non-invasive manner. Micro-beam Laue diffraction is based on the classical Laue diffraction approach where a crystalline sample is illuminated with a polychromatic X-ray beam. The resulting diffraction pattern consists of a large number of Laue diffraction peaks which give information about the lattice orientation and the distortion of the unit cell [67, 87, 88].

Scientific understanding obtained from experimental characterisation can be used to develop a numerical model of the irradiated material. Such material models can be used to numerically simulate the mechanical behaviour of similarly irradiated engineering components through for example crystal plasticity finite element simulations (CPFE) [89–93]. By constraining dislocation-mediated plasticity to specific slip directions, consistent with the crystallographic geometry of the material, CPFE renders a physical basis to predictions and makes them directly comparable to experimental observations [94–96]. Also important qualitative insight into the interaction mechanism between defects/precipitates and dislocations, such as irradiation-softening [97] or crack nucleation [98] can be obtained from such simulations. These models can be further enhanced by explicitly accounting for the dynamics of interaction between the population of radiation defects and gliding dislocations and the resultant evolution of the material microstructure and density of mobile or immobile dislocations [91, 99, 100].

## 5 Characterising irradiation damage in tungsten

### 5.1 Neutron irradiation damage

Using molecular dynamics simulations, Troev et al. [74] estimated the radiation damage produced by displacement-cascade in tungsten irradiated with neutrons. For a neutron fluence of  $2.5 \times 10^{22}$  n/cm<sup>2</sup>, they calculated a dpa of 2.85 in tungsten per full power year (FPY). At energies below 100 keV, at early stages after irradiation, interstitial volume was found to be twice larger than the volume of vacancies. The defect population was seen to be comprised of single vacancies, di-vacancies, interstitials and interstitial clusters containing more than 3 atoms.

Transmission electron microscopy (TEM) on self-ion-irradiated tungsten and its alloys with tantalum, vanadium and rhenium, exposed to different damage levels, has provided useful insights about the evolution of the defect morphology and population, in the neutron-irradiated reactor component, as a function of dose, temperature and presence of transmutation elements [10, 60, 61, 101]. For example, Yi et al. [101] studied tungsten (W) irradiated in situ by tungsten ions at 30 K (temperature where defect mobility is restricted) and showed that a power law can be used to explain the loop size distribution in cascades. In a follow-up study, Yi et al. [61] examined tungsten irradiated with self-ions at 150 keV, at temperatures between 30 and 1073 K, with doses between  $10^{16}$  to  $10^{18}$  W<sup>+</sup>m<sup>-2</sup> and ~25 nm thick irradiated layer. It was seen that the first observable defects (predominantly  $\frac{1}{2}\langle 111 \rangle$  vacancy loops) appear at doses < 0.01 dpa [61]. The concentration of retained defects was found to reduce with increasing temperature, with a simultaneous increase in cluster size, owing to defect cluster migration and elastic loop interaction. An example of the changing defect microstructure with temperature, in tungsten irradiated up to 0.1 dpa is shown in Fig. 4. While the loop morphology was found to change with temperature, Yi et al. observed that in the temperature range 30–1073 K, between 0.1 and 1 dpa, the number density of loops saturates in the range  $\sim 10^{15}$  loops/m<sup>2</sup>. Such analysis is important to understand the behaviour of radiation damage and their evolution as will take place in the high temperature environment in the fusion reactor.

Indeed several studies have focussed on investigating the recovery behaviour of the displacement damage induced by neutron irradiation which underlies the evolution of the defect microstructure. It is particularly useful to employ TEM for these studies, as by virtue of providing direct information about the nature of defects it can help quantify the time and temperature dependence of

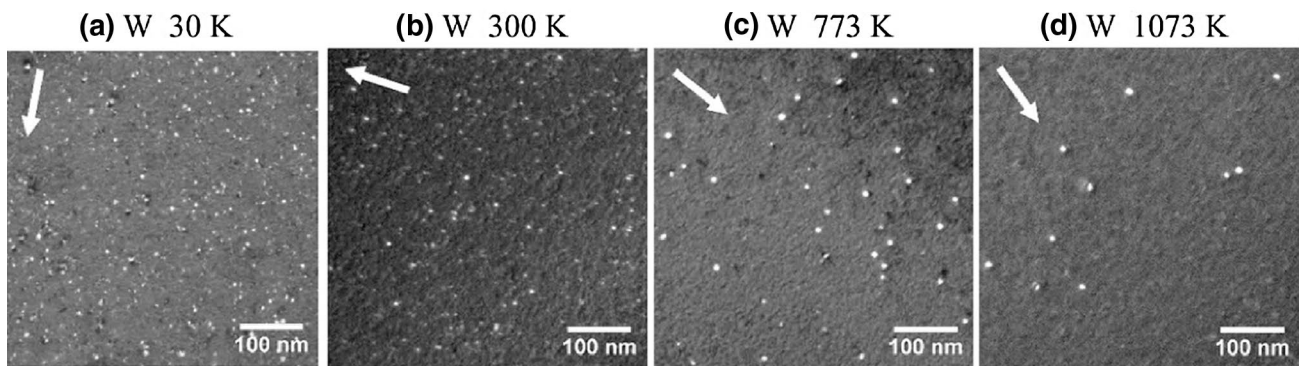


**Fig. 4** Defect microstructures in pure tungsten exposed to 0.01 dpa damage level, as a function of temperature from Stage I (30 K) to Stage IV (1073 K). The micrographs were recorded under weak-beam dark-field condition ( $g=200$ , 3–4  $g$ ) [61]

defect recovery. For example, Ferroni et al. [62] performed a detailed characterisation of defect microstructure in self-ion irradiated tungsten (2 MeV W<sup>+</sup> ions, 500 °C, 1014 W<sup>+</sup>/cm<sup>2</sup>), after high temperature (1073–1673 K) isochronal and isothermal annealing. Similar to the observation made by Yi et al., here too an increase in loop size (large oblong, finger loops formed by coalescence of smaller loops) and decrease in loop density was found with increasing temperature. At temperatures > 1273 K, dislocations were found to interact with small defect networks, “sweeping” out damage [62]. While loops at low temperatures are found to have Burgers’ vectors of  $a/2\langle 111 \rangle$  and  $\langle 100 \rangle$ , at temperature > 1073 K,  $a/2\langle 111 \rangle$  loop geometry was found to be the most thermally favoured [61]. Resistivity measurements have also been commonly used to examine the recovery behaviour of irradiation defects [102–104]. For example, Keys and Moteff used the resistivity technique to study in detail the recovery of defects in tungsten irradiated by > 1 MeV neutrons, at 340 K, with a fluence range of  $10^{17}$ – $10^{21}$  nm<sup>-2</sup>. Defect recovery below 770 K was found to be dominated by migration of self-interstitials, while that > 770 K was attributed to di-vacancy and tri-vacancy migration [102].

Thus, temperature and fluence play a vital role in determining the characteristics of the retained defect microstructure and finally on the mechanical properties which are altered by these defects. The influence of the retained defect microstructure on the mechanical properties are commonly investigated using micro-mechanical tests like nano-indentation and micro-cantilever tests. Nano-indentation on tungsten (ultra-high pure (UHP)) implanted at 300 °C with 2 MeV tungsten ions showed a saturation in hardness beyond ~0.4 dpa (~0.8 GPa or 11% hardness increase) as shown in Fig. 5a [80]. Also the loop number density was seen to saturate between 0.4 and 33 dpa [80]. Tungsten samples, self-ion implanted at higher temperatures, show higher hardness. For example, in tungsten samples implanted

with self-ions to ~2 dpa at 800 °C, ~20% increase in hardness was observed through micro-cantilever (example of a micro-cantilever shown in Fig. 5b) bending tests (loaded to failure under displacement control at a rate of 5 nm s<sup>-1</sup>) [79].

Fusion neutron irradiation can result in the formation of transmutation elements such as rhenium, osmium, tantalum [13]. Ion-irradiation of tungsten alloyed with either of these elements can be used to specifically investigate the effect of these transmutation elements on cascade damage behaviour. As such, self-ion implanted tungsten alloys with rhenium or tantalum have been used in several nano-indentation studies. Contrary to self-ion implanted tungsten which saturated in hardness beyond 0.4 dpa at 300 °C, self-ion implanted W-5wt%Re samples showed ~13% hardness increase up to 1.2 dpa and then a further increase of 20% and 40% at 13 and 33 dpa [80]. These massive increases in hardness are thought to be induced by formation of rhenium clusters which may be precursors of the sigma phase formation [80]. In self-ion implanted W-5wt%Ta alloy, a different trend is noticed. Large increase of ~21% in hardness is noticed for 0.07 dpa damage, but thereafter the hardness increase is less than 14% and saturates beyond 13 dpa [77]. Further, surprising observations of suppressed pile-up around Berkovich indents in these samples, for damage levels 0.07 dpa and 1.2 dpa, is made in contrast to the large pile-up seen around indents in unimplanted tungsten [77]. A plausible explanation for this observation and the different increases in hardness induced by tantalum and rhenium for low doses like 1.2 dpa are yet to be examined.

To sum up, cascade damage induced lattice defects in tungsten cause significant changes in hardness associated with a loop-dominated defect microstructure. The presence of alloying elements is found to further aggravate the radiation damage effects. However the underlying reasons for these observations, i.e. the mechanism of interaction of the induced defects (predominantly loops) with gliding



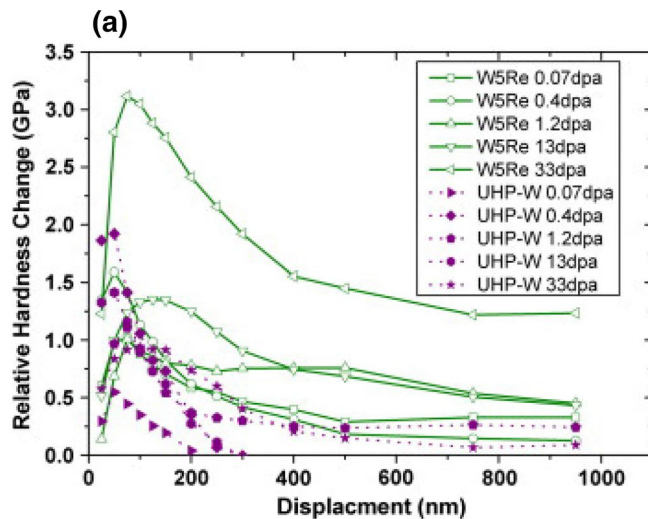


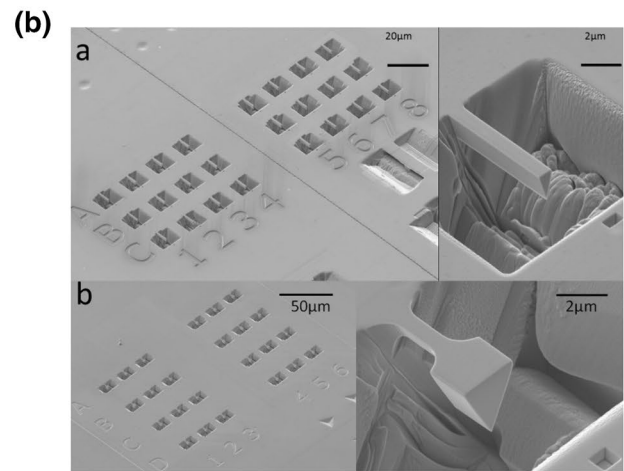
**Fig. 5 a** Relative increase in hardness as a function of depth for UHP-W and W5Re implanted to 0, 0.07, 0.4, 1.2, 13 and 33 dpa. A maximum increase in hardness is seen at 125 nm for all doses in

dislocations, as a function of dose and temperature, needs further exploration. Considering the expense and the lengthy process of neutron irradiation, ion irradiation is a practical choice for studying cascade damage models. However, predictive data collected from material irradiated with ions (or fission neutrons), cannot be directly used to represent fusion conditions [105]. Differences in terms of PKA recoil spectrum, transmutation and displacement rates must be analysed. Also the effect of environmental parameters such as stress state, flux pulsing and temperature, must be accounted for if the acquired data is to be used for designing fusion devices.

## 5.2 The effect of hydrogen on the plasma-facing component

Hydrogen and helium will be injected into the plasma facing component directly from the fusion plasma. Further, they can also be produced through the nuclear reactions i.e. transmutation [106].

Changes in physical and mechanical properties of tungsten, that can be induced by hydrogen (and its isotopes), depends largely on the amount of deuterium retained in the material. Generally in tungsten, the retention of hydrogen (and its isotopes) is very low. This is particularly true for implantation doses of less than  $10^{22}$  ions/m<sup>2</sup> [107]. In these cases, thermal desorption experiments showed that the majority of deuterium is desorbed between 400 and 600 K [107]. The low retention is partly caused by the high diffusivity of hydrogen in tungsten which allows the injected hydrogen to easily reach the surface and be released back into the plasma chamber [108]. Further, DFT



both material types [80]. **b** SEM images of arrays and typical micro-cantilevers with **a** a uniform cross-section and **b** waisted section [140]

modelling has shown that for small interatomic distances, the H–H state is unstable (at close distance, there is an asymmetric shift of the bonding and anti-bonding state, towards higher energy, thus increasing the interaction energy and resulting in weak repulsion instead of attraction) [75]. This implies that for doses less than  $10^{22}$  ions/m<sup>2</sup>, in an otherwise perfect matrix, hydrogen cannot form stable clusters on their own and cause bubble or blister formation.

However, at high implantation doses ( $> 10^{22}$  ions/m<sup>2</sup>), even low energy (at sub threshold energy of 38 eV, where the threshold for displacement damage is around 1 keV) implantation of deuterium ions into the material can create trapping sites in the sub-surface layer (within 2 μm) and sometimes up to few microns into the material [108]. It is argued that at such high fluence, the concentration of deuterium ions in the implanted layer (decided by the ion range) far exceeds the solubility limit, creating stress in the tungsten matrix and causing bubble and void formation by plastic deformation [109]. The surface topography decorated with blister formation is found to change as a function of temperature and grain orientation [110]. The stresses created by the high concentration of deuterium ions (at this high fluence range) can exceed the fracture toughness of tungsten, resulting in the formation of cracks [111]. At room temperature, near-surface small intergranular cracks are seen, which increase in length with increase in temperature. For temperatures below the BDTT, cracking within the grains is observed, while beyond the BDTT, cracking is reduced and large cavities are seen forming along the grain boundaries, up to few microns beneath the surface [108]. However for temperatures  $> 700$  K, no

significant surface changes or blister formation is noticed, even for high dose deuterium implantation. The authors hypothesize that at this high temperature, the significantly increased diffusivity, prevents the build-up of a transient high concentration of deuterium in the implanted layer. This is argued to prevent the stress which is required for the surface deformation. With further annealing of defects in tungsten at these high temperatures, stress and strain for defect formation is reduced, lowering blister formation is greatly [108].

Deuterium retention and its consequent effects not only vary with fluence but also with the defect density present in the tungsten substrate. Intrinsic defects in the material such as grain boundaries, dislocations, thermal vacancies, pores, inclusions etc. can act as trapping sites for hydrogen. The amount of hydrogen retained by such sources of course largely depends on the material purity, pre-treatment etc. [109]. The depth at which the deuterium is retained depends on the temperature, where beyond 400 K deuterium is found to diffuse to the bulk ( $> 5 \mu\text{m}$  depth) [108]. The defect density in the material can be increased by irradiation damage which can thereby increase the deuterium retention [109].

For instance, the presence of helium defects in tungsten can affect its deuterium retention capacity. Iwakiri et al. [107] irradiated tungsten with 8 keV helium at room temperature, followed by 8 keV deuterium at several temperatures (300–673 K). It was found that at 473 K, for a high dose of helium ( $2 \times 10^{21}$  ions/m<sup>2</sup>), a large number of small helium bubbles form effective trapping sites for deuterium. Thus, the deuterium trapping was three times greater than without helium pre-irradiation. Lee et al. also looked at the case for simultaneous irradiation of polycrystalline tungsten with hydrogen and helium (500 eV He<sup>+</sup> and D<sup>+</sup> (H<sup>+</sup>) ions with fluences of  $10^{21}$ – $10^{23}$  He<sup>+</sup>/m<sup>2</sup> and  $0.5$ – $2 \times 10^{23}$  D<sup>+</sup>(H<sup>+</sup>)/m<sup>2</sup> at 300 K [112]. It was seen that deuterium retention is increased by ~30%, particularly in the near surface (within 50 nm), due to the presence of trapping sites in the form of helium-induced defects.

Deuterium retention is also seen to change in presence of defects created by neutron or ion irradiation. Oya et al. [113] compared the desorption spectra from pure tungsten exposed to deuterium plasma (W–D) (fluence  $\sim 10^{25}$  D<sup>+</sup>m<sup>-2</sup> at 473 K) with that from tungsten implanted with Fe<sup>2+</sup> ions (0.025 dpa at 2.8 MeV) followed by exposure to deuterium plasma (W–Fe–D) (similar conditions as before). The deuterium desorption spectra showed only one prominent peak at 550 K for pure tungsten, but an additional peak at 450 K in ion-irradiated tungsten [113]. A further examination of the deuterium desorption spectra from tungsten irradiated by neutrons (0.025 dpa), followed by exposure to deuterium plasma (W–n–D) showed a third peak at 750 K. The authors hypothesise that the single

peak noticed in the desorption spectrum from pure tungsten arises from deuterium trapped at the intrinsic defects. Two peaks seen in the ion-irradiated case is considered to occur due to the irradiation defects trapping deuterium with different activation energies [113]. Finally, the three desorption stages in the neutron irradiated case is proposed to be caused by deuterium trapped in bulk of the material by neutron-induced defects, rather than only in the near surface region where the ion-irradiation defects are localised.

Interestingly a recent study shows that the deuterium retention will be even higher when simultaneous implantations are performed as may happen in-service during the reactor operation. Markelj et al. [114] compared deuterium retention in tungsten samples sequentially implanted with tungsten ions and deuterium with the retention in tungsten simultaneously implanted with deuterium and tungsten ions. Examining a range of temperature, Markelj et al. [114] concludes that between 300 and 1000 K, deuterium retention in simultaneously implanted samples is almost a factor of two higher than in the sequentially implanted case.

In terms of mechanical properties, retained deuterium can bring about reduced pop-in load and increase in hardness (maximum increase of 0.5 GPa) as observed by nano-indentation of tungsten exposed to deuterium plasma at 443 K, with incident ion energy of 35 eV and accumulated fluence of  $8.1 \times 10^{25}$  ions/m<sup>2</sup> [15]. Similar observations of increased hardness were made by Terentyev et al. [115] and Zayachuk et al. [116] in tungsten exposed to deuterium plasma. Overall, observations from past studies clearly indicate that despite the fast diffusion of hydrogen isotopes at fusion relevant temperatures, a significant percentage of the injected ions will be trapped by irradiation defects. This change in the retention of hydrogen is found to not only depend on defects created by prior irradiation, but also on the synergistic effects as takes place when there is simultaneous irradiation of hydrogen and neutron/helium. These changes need to be carefully accounted for in the reactor design to correctly evaluate the behaviour of hydrogen isotope and its ultimate effect on the mechanical properties of the tungsten component in-service in the reactor.

### 5.3 The effect of helium on the plasma-facing component

In the armour component, little helium is formed through transmutation, and it would take more than 300 years for any significant embrittlement through transmuted helium [12]. Thus the main source of helium will be that implanted from the fusion plasma. Helium-induced damage in tungsten is complex and varies with fluence, implantation

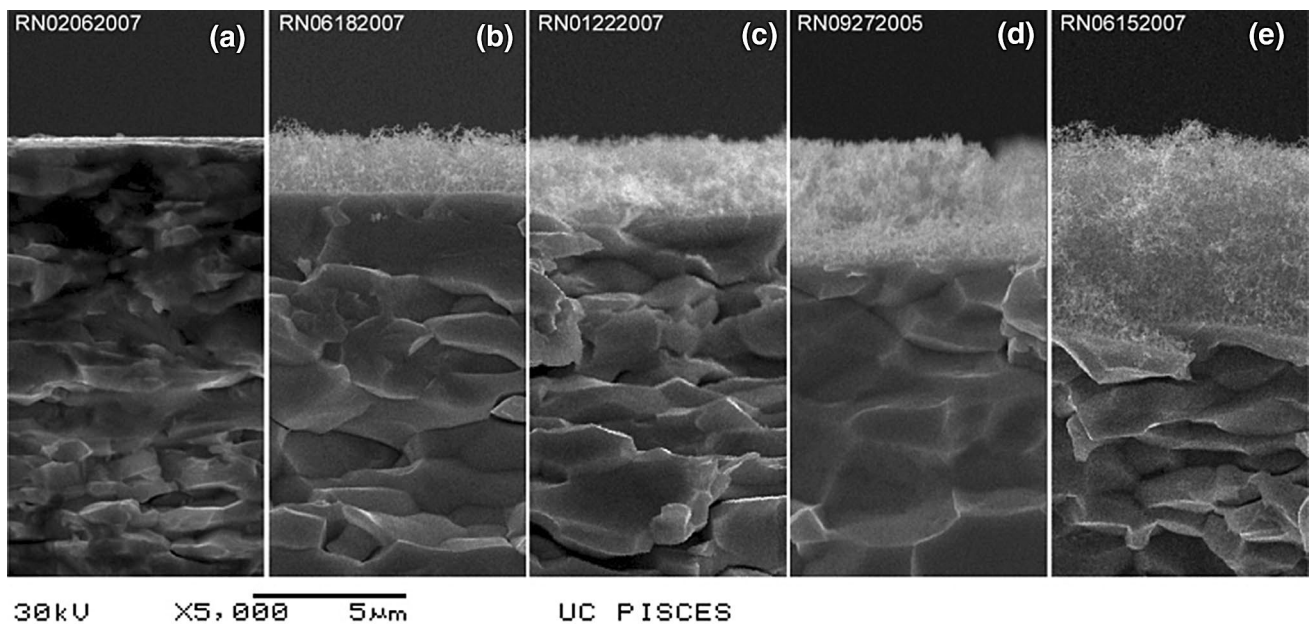


**Fig. 6** Cross-sectional SEM images of W targets exposed to pure He plasma for exposures times of **a** 300 s, **b**  $2.0 \times 10^3$  s, **c**  $4.3 \times 10^3$  s, **d**  $9.0 \times 10^3$  s and **e**  $2.2 \times 10^4$  s. Targets were exposed at a fixed temperature of 1120 K. The plasma properties varied

slightly in the parameter ranges  $n_e = 4 \times 10^{18} \text{ m}^{-3}$  and  $T_e \sim 6\text{--}8 \text{ eV}$ ,  $\Gamma_{\text{He}^+} = (4\text{--}6) \times 10^{22} \text{ m}^{-2} \text{ s}^{-1}$  in order to maintain the constant fixed target temperature [122]

energy and implantation temperature. It is also influenced by the amount of helium retained. Grain boundaries act as trapping sites for helium and thus the helium retention is more in polycrystalline tungsten than in single crystals where the lack of trapping sites, allows long range diffusion of helium during annealing [117].

DFT calculations show that the stable interstitial site for the retained helium is the tetrahedral site and at close separation He–He binding is strong through pure elastic interaction [75]. This enables helium to form stable clusters even in a defect free crystal. When the interstitial helium cluster gets large, it displaces metal atoms from their lattice site to release the pressure generated by the helium atoms [75]. Frenkel pair defects are formed by this mechanism, which is called trap mutation.

Besides forming strong interactions with themselves (1.01 eV), helium interacts strongly with defects generated, such as vacancies (4.57 eV), vacancy clusters and impurities [118]. The helium-vacancy bond is particularly strong [119] and DFT calculations showed that mobile vacancy clusters which disintegrate at fusion temperatures, are stabilized by helium atoms which reduces the vacancy emission rates [75]. The helium-vacancy bond which makes the vacancies immobile, can also influence void formation induced by ion-irradiation. Yoshida et al. [118] found that dense interstitial loops and fine voids induced by  $\text{Cu}^+$  implantation in tungsten (at 2.4 MeV to

3 dpa), almost disappears in presence of helium (0.25 keV at  $10^{22} \text{ He}^+/\text{m}^2$ ).

At temperatures below 873 K, helium vacancy complexes with their low thermal migration, form dense fine helium bubbles, by absorbing more and more helium. Besides bubbles, blistering can be formed, when the highly pressurized fine bubbles, formed close to the projected range of the incident ions, mediate inter bubble cracking [118]. At higher temperatures (1073–1273 K), when vacancies and helium bubbles can migrate thermally, large helium bubbles form [118, 120]. With increase in helium fluence and temperature, bubbles can evolve into ‘nanofuzz’ structures (generally forming between 1000 and 2000 K) as shown in Fig. 6 [120–122]. It has been seen that presence of hydrogen and carbon in the helium plasma, can lower the fuzz formation [120]. Since the conditions of fuzz formation are very similar to the conditions that the armour component will be exposed to in-service in the reactor, significant research efforts continue to be made to understand the mechanism of its formation and possible means of inhibiting its formation.

Even low energy helium ion implantation can cause surface modifications in tungsten (with a displacement threshold energy of 42–44 eV, depending on the crystallographic direction). For example, Nishijima et al. [123] observed micron sized surface pores in tungsten implanted with as low as 10 eV helium ions at 1600 K. For 19 keV helium implanted at  $\sim 800^\circ \text{C}$ , large blisters were

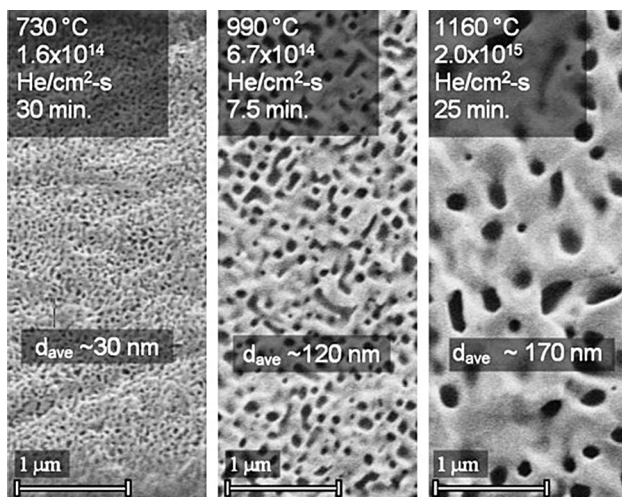


**Fig. 7** Micrographs of tungsten surfaces implanted with 30 keV He [125]

seen to form [124]. Cipiti et al. [125] also observed that 30 keV helium implanted between 730 and 1160 °C with doses of about  $\sim 3 \times 10^{22} \text{ m}^{-2}$ , interacted with vacancies, to form large helium bubbles and numerous surface pores. Figure 7 shows the formation of these bubbles and pores on the tungsten sample, with diameter ranging from 15 to 150 nm (increasing diameter and reduced density with increasing temperature) [125]. Similar results of a sub-surface semi-porous layer, was observed in polycrystalline tungsten samples, irradiated with 30 keV helium, at temperature range of 500–900 °C, [126]. The layer was found to reach up to 1000 nm below surface for fluence of about  $10^{23} \text{ He/m}^2$ .

Helium-defects can significantly impact tungsten's deformation behaviour. High temperature nano-indentation of tungsten samples implanted with  $\sim 600$  appm of helium showed hardness increase (averaged between 150 and 400 nm penetration depth) of about 14% at 330 K and 55% increase at 523 K [17]. However, beyond 700 K, no such significant hardness increase is witnessed [17]. Figure 8c shows this change in helium-defect induced hardness as a function of temperature. Even the small helium-induced defects formed at room temperature (few-atom-large V and SIA clusters [127, 128]), can cause a substantial increase in material hardness, degradation of thermal diffusivity and embrittlement [129, 130]. Injected helium concentrations of 0.3 at% (at 300 K) has been seen to cause 30% increased hardness [78] and 50% reduction of room temperature thermal diffusivity [130]. Further, contrary to suppressed pile-up around indents in self-ion implanted tungsten [77], large pile-up was seen around 250 nm deep Berkovich nano-indents in these samples. The significantly increased pile-up around indents in

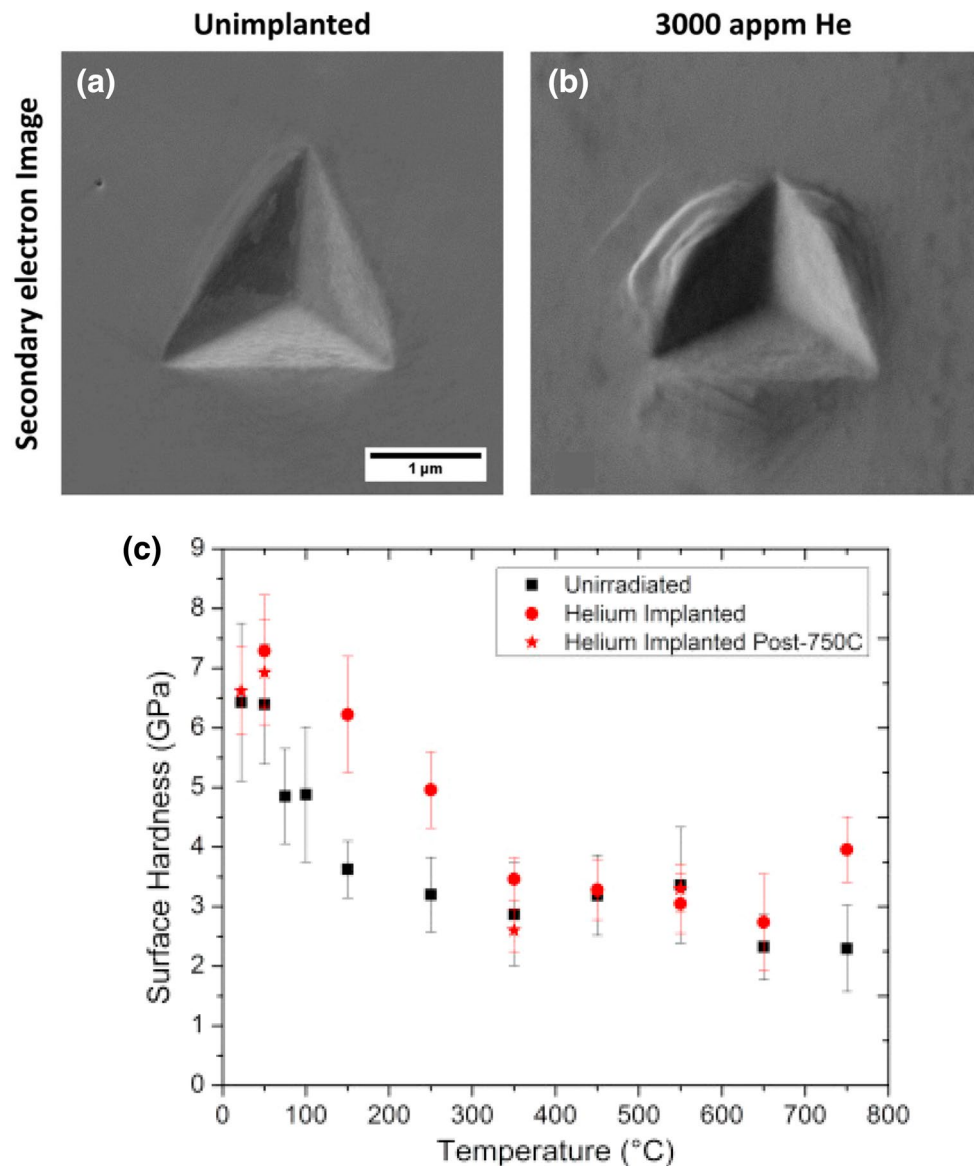
helium-implanted tungsten is shown in Fig. 8a and b, which compares the indents in pure tungsten with that in helium-implanted tungsten. Similar observations of large pile-up were also made around 500 nm deep spherical nano-indents in  $\langle 001 \rangle$ -oriented W-0.3wt% He [58, 78]. This implies that the underlying mechanism of interaction of dislocations with helium-defects is different from that with self-ion implantation induced defects. To obtain a coherent understanding of this, different methods have been applied to probe the small helium-defects formed at low temperature ( $\sim < 573$  K). These defects were found to remain undetected by high-resolution TEM (1.5 nm resolution) [63, 129]. The defects were subsequently attempted to be probed by measuring the lattice strains they cause.

For example, micro-Laue diffraction was used to measure the strain in W-1%Re alloy, implanted with 3110 appm helium at 573 K [48]. Significant lattice swelling, resulting in an out-of-plane strain of  $1.5 \times 10^{-3}$  was measured in the approximately 2.7  $\mu\text{m}$  implanted layer. By relating the corresponding hydrostatic strain of  $2.62 \times 10^{-3}$  with DFT calculations, the study showed that helium vacancy clusters most probably contain a pair of helium atoms. With increase in temperature to 1473 K, the helium-induced lattice swelling was found to extend beyond the implanted layer, suggesting that thermal activation enhances defect migration into the material [14].

The competence of X-ray Laue diffraction in probing the small (few atom large) defects induced by helium-implantation has been extended to explore other aspects of helium irradiation damage, such as change in defect retention with dose or change in irradiation induced deformation behaviour. For example, Laue diffraction measurements performed on 300 and 3000 appm helium-implanted tungsten samples showed an increase volumetric strain by only  $\sim 2.4$  times, suggesting that defect retention per injected helium atom is  $\sim 3$  times higher at low doses. [69]. This implies that retention of defects may not be a simple function of implanted helium dose, but can strongly depend on material composition and presence of impurities. This change in defect retention as a function of irradiation dose or presence of impurities, is particularly important in order to accurately estimate irradiation-induced residual stresses that can affect the fatigue performance of the components. Analysis of helium-implanted W-1wt% Re alloy samples, of different crystal orientations and with varying implantation doses, in a similar manner (through strain measurements from diffraction) showed that both the presence of rhenium, and crystal orientation, have a relatively small influence on defect retention [69].

Such high resolution strain measurements have also helped gain insight into the underlying mechanism by which these small defects induce significant change in tungsten's deformation behaviour. 3D-resolved X-ray

**Fig. 8** **a, b** SEM images of 250 nm deep indents in unimplanted and He+ implanted sample respectively [78]. **c** Nano-indentation hardness from shallow indents (averaged between 150 and 400 nm) for an unirradiated sample and the helium-implanted sample [17]

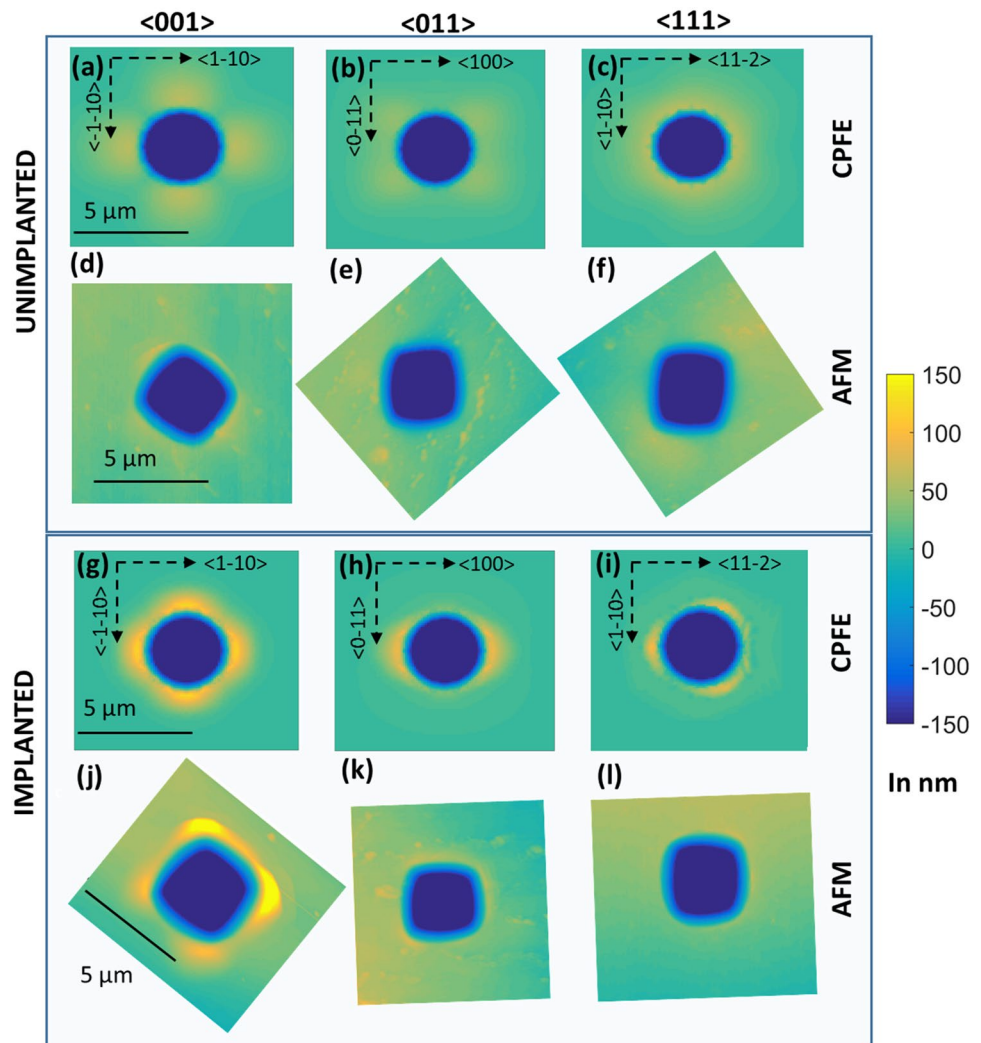


micro-diffraction measurements around spherical nano-indentations in  $\langle 001 \rangle$ -oriented W-0.3wt% He (implanted at 300 K) showed a more confined plastic zone under indents as compared to that observed under similar indents in pure tungsten [58]. Localised deformation and slip-channel formation in W-0.3wt% He (implanted at 300 K) was also confirmed through HR-EBSD and TEM on cross-section lift-outs from indents [89]. The authors suggest that the interaction of dislocations with helium-defects involves a large initial hardening due to helium-defects, followed by localised defect removal and subsequent strain softening [58]. Such irradiation-induced softening has been noted before in irradiated materials such as neutron-irradiated copper [131, 132], neutron-irradiated vanadium [133], self-ion irradiated stainless steel [134, 135], and neutron-irradiated pure Fe [136].

Consequently a CPFÉ simulation of indentation in  $\langle 001 \rangle$ -oriented W-0.3wt% He was developed based on the theory of irradiation-induced strain-softening [90]. With only one fitting parameter the formulation could capture the localised large pile-up and predict confined fields of lattice distortions beneath indents in quantitative agreement with experimental measurements, confirming the accuracy of the proposed theory [90].

Surprisingly however, while 500 nm deep spherical nano-indentations in  $\langle 001 \rangle$ -oriented W-0.3wt% He showed large pile-up and slip steps [58], similar indents made in  $\langle 011 \rangle$  and  $\langle 111 \rangle$  grains of the sample helium-implanted tungsten sample showed negligible pile-up [90]. Figure 9j–l shows this experimentally observed orientation-dependence of pile-up pattern in helium-implanted tungsten. The CPFÉ formulation discussed above (i.e. the one

**Fig. 9** Surface profiles of residual out-of-plane displacement after indentation. CPFE simulations for the unimplanted (a–c) and the helium-implanted sample (g–i) for  $\langle 001 \rangle$ ,  $\langle 011 \rangle$  and  $\langle 111 \rangle$  out-of-plane crystal orientations respectively. AFM for the unimplanted (d–f) and the helium-implanted sample (j–l) for  $\langle 001 \rangle$ ,  $\langle 011 \rangle$  and  $\langle 111 \rangle$  out-of-plane crystal orientations respectively. The AFM micrographs have been rotated to match the in-plane orientations as labelled on the CPFE plots. The colour scale and 5  $\mu\text{m}$  scale bar are the same for all plots [90]



built from experimental observations made in the indent in  $\langle 001 \rangle$ -oriented grain in W-0.3wt% He), was successful in capturing the orientation dependence of pile-up pattern as shown in Fig. 9g–i. Importantly, this suggests that the underlying strain localisation is orientation-independent and that changes in pile-up arise due to the relative orientations of slip systems, sample surface, and the indenter [90].

The observations from all of the reviewed studies examining helium irradiated tungsten, highlight the detrimental changes in the properties of tungsten that will be induced by the helium-irradiation defects. Interestingly, however, a recent study by Guo et al. has shown a potential benefit associated with the presence of such helium-induced defects. The operation window for tungsten components in the fusion reactor is 800–1300  $^{\circ}\text{C}$  [18]. The upper limit of this window is limited by the recrystallization temperature of tungsten. Recrystallization is unfavourable for the tungsten components, as tungsten becomes less ductile post recrystallization [137]. This increased brittleness of

recrystallized tungsten is largely attributed to the formation of high angle grain boundaries [137]. Guo et al. [138] observed that when annealing tungsten, which has been exposed to helium plasma at  $\sim 550$ –600 K ( $\sim$  fluence of  $10^{26} \text{ m}^{-2}$ ), the recrystallization stage was retarded up to few microns beneath the surface (fully recrystallized at 1673 K compared to pure tungsten which fully recrystallized at 1473 K). Grain growth stage was also found to slow down in helium exposed tungsten and differences in average grain size between pure tungsten and helium-implanted tungsten was found to remain even after annealing up to 1973 K. The observation was mainly attributed to the retarded migration of high angle grain boundaries in presence of helium clusters and bubbles and implies that presence of helium-irradiation defects in-service, in the tungsten armour component, may help by increasing the upper limit of the operation temperature window [138].

In summary, helium induces prominent changes in tungsten's microstructure which can influence the deuterium retention and evolution of neutron-induced void

swelling. Unlike hydrogen, helium forms a stable bond with itself and helium clusters are strong enough to create lattice defects. At room temperature, helium bonds strongly with vacancies and these few atom large clusters can induce significant lattice swelling and alarming alterations in tungsten's mechanical properties. A combination of experimental and computational crystal plasticity modelling was able to confirm that the mechanism underlying these surprising changes involves irradiation hardening followed by subsequent strain-softening; a mechanism which is orientation-independent. Such studies also inspire confidence in the predictive ability of physically-based computational models, which can capture the physics of irradiation-induced changes as understood from multi-technique experimental observations.

To develop comprehensive predictive models, which are relevant to fusion operation conditions, future research entails detailed characterisation of helium-defects as a function of the factors such as

1. Temperature—thermal activation can enhance defect mobility (into the bulk) and defect morphology (bubble and blister formation).
2. Irradiation conditions—fluence and energy changes can alter the defect microstructure (bubbles evolving into nanofuzz).
3. Grain sizes—Smaller grain sizes i.e. more grain boundaries can act as defect nucleation sites and increase helium retention.

Such characterisation performed using a combination of complementary experimental techniques at multiple length-scales is essential to understand the mechanism underlying time, fluence, temperature and material property (impurity content, grain sizes etc.) dependent damage evolution and its ultimate impact on the structural and functional properties of the armour component. A complete scientific understanding gained from such multi-technique and multi-scale experimental observations can then be used to link experimental observations to physically-based parameters and develop predictive numerical models representative of the experimentally characterised irradiated material. Without such numerical models, the macroscopic behaviour of similarly irradiated materials is challenging to examine (in most instances a few micron thick implanted layer is investigated experimentally and translating these observations to macro-scale components, with reactor relevant dimensions, is possible through modelling efforts such as dislocation-dynamics integrated strain-gradient crystal plasticity models, which accounts for the size-effect). Only with

the development of such models can successful predictions of the structural integrity and performance of tungsten armour components (of fusion relevant dimensions) be made. These predictions are essential for the design of future fusion reactors beyond ITER.

## 6 Summary

This paper reviewed recent advances in the understanding of irradiation damage in tungsten, the main candidate material for armour components in future fusion reactors. Ion implantation is commonly used to mimic the radiation damage that tungsten components will experience in-service. Despite limitations, ion-implantation has been shown to be an effective technique to enable isolated investigation of damage effects, up to high damage levels (of tens of dpa), without the added complexity of transmutation and material activation. Further, this provides a convenient way of simultaneously mimicking damage formed by energetic neutron irradiation and introducing gaseous elements into the tungsten matrix so that its interaction with defects may be studied. Study of ion-implanted materials using a combination of experimental and modelling techniques, has helped gain important insights about irradiation induced dimensional change, the mechanism of interaction of irradiation defects with mobile dislocations and consequent changes in mechanical properties.

It has been seen that tungsten will be embrittled by neutron irradiation as a result of radiation hardening. Helium is anticipated to worsen this problem, owing to its low solubility in the crystal lattice and its affinity for lattice defects, particularly vacancies. Helium-implantation induced defects at room temperature, which remain "invisible" in TEM, have been shown to be effectively probed by measuring the lattice strains induced by them. Nano-indentation measurements have shown that both helium-ion implantation and self-ion implantation can induce significant hardening along with pile-up and suppression of pile-up around indents respectively. Nano-indentation measurements have also shown that helium-ion implantation had a much greater effect on hardness than collision cascade damage caused by self-ion implantation, suggesting that the presence of helium enhances defect retention and/or increases obstacle strength.

The alterations induced by the irradiation defects such as increased hardness and reduced work hardening capacity are detrimental to material ductility, a key concern for long-term structural integrity of future tungsten-based diverter concepts. Recent developments of physically-based models that capture the physics underlying irradiation-induced changes are promising and inspire confidence that in future it may be feasible

to reliably predict mechanical behaviour and in-service performance of irradiated engineering components through numerical simulations. This is key for the optimal design of fusion armour components and the overall commercial realisation of the fusion reactor.

**Acknowledgments** This work was funded by Leverhulme Trust Research Project Grant RPG-2016-190.

## Compliance with ethical standards

**Conflict of interest** The corresponding author states that there is no conflict of interest.

**Open Access** This article is distributed under the terms of the Creative Commons Attribution 4.0 International License (<http://creativecommons.org/licenses/by/4.0/>), which permits unrestricted use, distribution, and reproduction in any medium, provided you give appropriate credit to the original author(s) and the source, provide a link to the Creative Commons license, and indicate if changes were made.

## References

- U.S. Energy Information Administration, International Energy Outlook 2016, 2016. doi:[www.eia.gov/forecasts/ieo/pdf/0484\(2016\).pdf](http://www.eia.gov/forecasts/ieo/pdf/0484(2016).pdf)
- <https://www.euro-fusion.org/jet/jets-main-features/>, EUROfusion—Jet's main features, Webpage. (2019)
- <https://www.iter.org/proj/inafewlines>, What will ITER do?, Webpage. (2019)
- Bolt H, Brendel A, Levchuk D, Greuner H, Maier H (2006) Materials for plasma facing components of fusion reactors. *Energy Mater Mater Sci Eng Energy Syst* 1:121–126. <https://doi.org/10.1179/174892406X144451>
- <https://www.iter.org/sci/whatisfusion>, What is Fusion?, Webpage. (2019)
- Rieth M, Dudarev SL, Gonzalez de Vicente SM, Aktaa J, Ahlgren T, Antusch S, Armstrong DEJ, Balden M, Baluc N, Barthe M-F, Basuki WW, Battabyal M, Becquart CS, Blagoeva D, Boldyryeva H, Brinkmann J, Celino M, Ciupinski L, Correia JB, De Backer A, Domain C, Gaganidze E, Garcia-Rosales C, Gibson J, Gilbert MR, Giuseppe S, Gludovatz B, Greuner H, Heinola K, Höschen T, Hoffmann A, Holstein N, Koch F, Krauss W, Li H, Lindig S, Linke J, Linsmeier C, López-Ruiz P, Maier H, Matejicek J, Mishra TP, Muhammed M, Muñoz A, Muzyk M, Nordlund K, Nguyen-Manh D, Opschoor J, Ordás N, Palacios T, Pintsuk G, Pippan R, Reiser J, Riesch J, Roberts SG, Romaner L, Rosiński M, Sanchez M, Schulmeyer W, Traxler H, Ureña A, van der Laan JG, Veleva L, Wahlberg S, Walter M, Weber T, Weitkamp T, Wurster S, Yar MA, You JH, Zivelonghi A (2013) Recent progress in research on tungsten materials for nuclear fusion applications in Europe. *J Nucl Mater* 432:482–500. <https://doi.org/10.1016/j.jnucmat.2012.08.018>
- Zayachuk Y, Hoen MHJ<sup>T</sup>, Zeijlmans Van Emmichoven PA, Terentyev D, Uytendhouwen I, Van Oost G (2013) Surface modification of tungsten and tungsten-tantalum alloys exposed to high-flux deuterium plasma and its impact on deuterium retention. *Nucl Fusion* 53:13013–13017. <https://doi.org/10.1088/0029-5515/53/1/013013>
- Sharafat S, Takahashi A, Nagasawa K, Ghoniem N (2009) A description of stress driven bubble growth of helium implanted tungsten. *J Nucl Mater* 389:203–212. <https://doi.org/10.1016/j.jnucmat.2009.02.027>
- Zinkle SJ, Was GS (2013) Materials challenges in nuclear energy. *Acta Mater* 61:735–758. <https://doi.org/10.1016/j.actamat.2012.11.004>
- Yi X, Jenkins ML, Briceno M, Roberts SG, Zhou Z, Kirk MA (2013) In situ study of self-ion irradiation damage in W and W-5Re at 500°C. *Philos Mag* 93:1715–1738. <https://doi.org/10.1080/14786435.2012.754110>
- Barabash V, Federici G, Rödiger M, Snead LL, Wu CH (2000) Neutron irradiation effects on plasma facing materials. *J Nucl Mater* 283–287:138–146. [https://doi.org/10.1016/S0022-3115\(00\)00203-8](https://doi.org/10.1016/S0022-3115(00)00203-8)
- Gilbert MR, Dudarev SL, Zheng S, Packer LW, Sublet JC (2012) An integrated model for materials in a fusion power plant: transmutation, gas production, and helium embrittlement under neutron irradiation. *Nucl Fusion* 52:83019. <https://doi.org/10.1088/0029-5515/52/8/083019>
- Gilbert MR, Sublet J-C (2011) Neutron-induced transmutation effects in W and W-alloys in a fusion environment. *Nucl Fusion* 51:43005. <https://doi.org/10.1088/0029-5515/51/4/043005>
- de Broglie I, Beck CEE, Liu W, Hofmann F (2015) Temperature dependence of helium-implantation-induced lattice swelling in polycrystalline tungsten: X-ray micro-diffraction and Eigenstrain modelling. *Scr Mater* 107:96–99. <https://doi.org/10.1016/j.scriptamat.2015.05.029>
- Fang X, Kreter A, Rasinski M, Kirchlechner C, Brinckmann S, Linsmeier C, Dehm G (2018) Hydrogen embrittlement of tungsten induced by deuterium plasma: insights from nanoindentation tests. *J Mater Res* 33:3530–3536. <https://doi.org/10.1557/jmr.2018.305>
- Lhuillier PE, Belhabib T, Desgardin P, Courtois B, Sauvage T, Barthe MF, Thomann AL (2011) Trapping and release of helium in tungsten. *J Nucl Mater* 416:13–17. <https://doi.org/10.1016/j.jnucmat.2010.12.042>
- Gibson JSK-L, Roberts SG, Armstrong DEJ (2015) High temperature indentation of helium-implanted tungsten. *Mater Sci Eng, A* 625:380–384. <https://doi.org/10.1016/j.msea.2014.12.034>
- Zinkle SJ, Ghoniem NM (2000) Operating temperature windows for fusion reactor structural materials. *Fusion Eng Des* 51–52:55–71. [https://doi.org/10.1016/S0920-3796\(00\)00320-3](https://doi.org/10.1016/S0920-3796(00)00320-3)
- Singheiser L, Hirai T, Linke J, Pintsuk G, Rödiger M (2009) Plasma-facing materials for thermo-nuclear fusion devices. *Trans Indian Inst Met* 62:123–128. <https://doi.org/10.1007/s12666-009-0016-y>
- Roth J, Tsitron E, Loarer T, Philipps V, Brezinsek S, Loarte A, Counsell GF, Doerner RP, Schmid K, Ogorodnikova OV, Causey RA (2008) Tritium inventory in ITER plasma-facing materials and tritium removal procedures. *Plasma Phys Control Fusion* 50:103001. <https://doi.org/10.1088/0741-3335/50/10/103001>
- Pestchanyi S, Safronov V, Landman I (2004) Estimation of carbon fibre composites as ITER divertor armour. *J Nucl Mater* 329–333:697–701. <https://doi.org/10.1016/j.jnucmat.2004.04.189>
- Raffray AR, El-Guebaly L, Federici G, Haynes D, Najmabadi F, Petti D (2017) Dry-wall survival under IFE conditions. *Fusion Sci Technol* 46:417–437. <https://doi.org/10.13182/fst04-a581>
- Ekman M, Persson K, Grimvall G (2000) Phase diagram and lattice instability in tungsten ± rhenium alloys. *J Nucl Mater* 278:276–279. [https://doi.org/10.1016/S0022-3115\(99\)00241-X](https://doi.org/10.1016/S0022-3115(99)00241-X)
- Wei N, Jia T, Zhang X, Liu T, Zeng Z, Yang X (2014) First-principles study of the phase stability and the mechanical properties of W-Ta and W-Re alloys. *AIP Adv* 4:57103. <https://doi.org/10.1063/1.4875024>



25. Gumbsch P (1998) Controlling factors for the brittle-to-ductile transition in tungsten single crystals. *Science* 282:1293–1295. <https://doi.org/10.1126/science.282.5392.1293>
26. Murty KL (1975) Chapter 3. Radiation damage. *Fundam Asp Nucl React Elem* 59: 1–6. <http://www4.ncsu.edu/~murty/NE509/NOTES/Ch3-RadiationDamage.pdf>
27. Zheng Y, Zuo Y, Yuan D, Zhou D, Xu Y, Fan P, Zhu J, Wang Z, Zhu S (2010) Investigation of radiation damage in stainless steel, tungsten and tantalum by heavy ion irradiations. *Nucl Phys A* 834:761c–763c. <https://doi.org/10.1016/j.nuclphysa.2010.01.139>
28. Tungsten uses, Int. Tungsten Ind. Assoc. (2011)
29. Giannattasio A, Roberts SG (2007) Strain-rate dependence of the brittle-to-ductile transition temperature in tungsten. *Philos Mag* 87:2589–2598. <https://doi.org/10.1080/14786430701253197>
30. Tran-Huu-Loi JP, Morniroli M, Gantois M (1985) Lohay, Brittle fracture of polycrystalline tungsten. *J Mater Sci* 20:199–206. <https://doi.org/10.1007/BF00555913>
31. Sanders WT (1962) Peierls stress for an idealized crystal model. *Phys Rev* 128:1540–1549. <https://doi.org/10.1103/PhysRev.128.1540>
32. Hertzberg (1976) Deformation and fracture mechanics of engineering materials, 4th ed
33. Caillard D, Martin J (2003) Thermally activated mechanisms in crystal plasticity, 1st ed. <https://www.elsevier.com/books/thermally-activated-mechanisms-in-crystal-plasticity/caillard/978-0-08-042703-4>
34. Gordon PA, Neeraj T, Li Y, Li J (2010) Screw dislocation mobility in BCC metals: the role of the compact core on double-kink nucleation. *Model Simul Mater Sci Eng* 18:85008. <https://doi.org/10.1088/0965-0393/18/8/085008>
35. Hirth JP, Lothe J (2016) Theory of dislocations. Cambridge University Press, Cambridge
36. Margevicius R, Riedle J, Gumbsch P (1999) Fracture toughness of polycrystalline tungsten under mode I and mixed mode I/II loading. *Mater Sci Eng, A* 270:197–209. [https://doi.org/10.1016/S0921-5093\(99\)00252-X](https://doi.org/10.1016/S0921-5093(99)00252-X)
37. Giannattasio A, Yao Z, Tarleton E, Roberts SG (2010) Brittle–ductile transitions in polycrystalline tungsten. *Philos Mag* 90:3947–3959. <https://doi.org/10.1080/14786435.2010.502145>
38. Romaner L, Ambrosch-Draxl C, Pippan R (2010) Effect of rhenium on the dislocation core structure in tungsten. *Phys Rev Lett*. <https://doi.org/10.1103/physrevlett.104.195503>
39. Huang C-H, Gilbert MR, Marian J (2018) Simulating irradiation hardening in tungsten under fast neutron irradiation including Re production by transmutation. *J Nucl Mater* 499:204–215. <https://doi.org/10.1016/j.jnucmat.2017.11.026>
40. Huang CH, Gharaee L, Zhao Y, Erhart P, Marian J (2017) Mechanism of nucleation and incipient growth of Re clusters in irradiated W-Re alloys from kinetic Monte Carlo simulations. *Phys Rev B* 96:1–18. <https://doi.org/10.1103/PhysRevB.96.094108>
41. Rieth M, Hoffmann A (2010) Influence of microstructure and notch fabrication on impact bending properties of tungsten materials. *Int J Refract Met Hard Mater* 28:679–686. <https://doi.org/10.1016/j.ijrmhm.2010.04.010>
42. Du J, Höschel T, Rasinski M, You J-H (2011) Shear debonding behavior of a carbon-coated interface in a tungsten fiber-reinforced tungsten matrix composite. *J Nucl Mater* 417:472–476. <https://doi.org/10.1016/j.jnucmat.2010.12.254>
43. He G, Xu K, Guo S, Qian X, Yang Z, Liu G, Li J (2014) Preparation of tungsten fiber reinforced-tungsten/copper composite for plasma facing component. *J Nucl Mater* 455:225–228. <https://doi.org/10.1016/j.jnucmat.2014.05.026>
44. Veleva L (2011) Contribution to the production and characterization of W-Y, W-Y2O3 and W-TiC materials for fusion reactors
45. Fan J, Han Y, Li P, Sun Z, Zhou Q (2014) Micro/nano composited tungsten material and its high thermal loading behavior. *J Nucl* 455:717–723. <https://doi.org/10.1016/j.jnucmat.2014.09.037>
46. Hardie CD, Williams CA, Xu S, Roberts SG (2013) Effects of irradiation temperature and dose rate on the mechanical properties of self-ion implanted Fe and Fe–Cr alloys. *J Nucl Mater* 439:33–40. <https://doi.org/10.1016/j.jnucmat.2013.03.052>
47. Morris JW (2007) Chapter 4 : defects in crystals. *Mater Sci pp* 76–107
48. Hofmann F, Nguyen-Manh D, Gilbert MR, Beck CE, Eliason JK, Maznev AA, Liu W, Armstrong DEJ, Nelson KA, Dudarev SL (2015) Lattice swelling and modulus change in a helium-implanted tungsten alloy: X-ray micro-diffraction, surface acoustic wave measurements, and multiscale modelling. *Acta Mater* 89:352–363. <https://doi.org/10.1016/j.actamat.2015.01.055>
49. Ciupiński Ł, Ogorodnikova OV, Płociński T, Andrzejczuk M, Rasiński M, Mayer M, Kurzydłowski KJ (2013) TEM observations of radiation damage in tungsten irradiated by 20 MeV W ions. *Nucl Instrum Methods Phys Res Sect B Beam Interact Mater Atoms* 317:159–164. <https://doi.org/10.1016/j.nimb.2013.03.022>
50. [http://ec.europa.eu/research/energy/euratom/index\\_en.cfm?pg=fusion&section=iter-future](http://ec.europa.eu/research/energy/euratom/index_en.cfm?pg=fusion&section=iter-future), ITER Future and DEMO, Webpage. (2019)
51. Vladimirov P, Möslang A (2004) Comparison of material irradiation conditions for fusion, spallation, stripping and fission neutron sources. *J Nucl Mater* 329–333:233–237. <https://doi.org/10.1016/j.jnucmat.2004.04.030>
52. Sekimura N (1996) Primary knock-on atom energy dependence of cascade damage formation and interaction. *J Nucl Mater* 233–237:1080–1084
53. Ryazanov AI, Metelkin EV, Semenov EV (2009) Modeling of cascade and sub-cascade formation at high PKA energies in irradiated fusion structural materials. *J Nucl Mater* 386–388:132–134. <https://doi.org/10.1016/j.jnucmat.2008.12.071>
54. Ryazanov AI, Semenov EV (2011) Radiation damage formation in fusion structural materials due to elastic and inelastic processes. *J Nucl Mater* 417:1074–1077. <https://doi.org/10.1016/j.jnucmat.2010.12.182>
55. De Backer A, Sand AE, Nordlund K, Luneville L, Simone D, Dudarev SL (2016) Subcascade formation and defect cluster size scaling in high-energy collision events in metals. *Europhys Lett* 115:26001. <https://doi.org/10.1209/0295-5075/115/26001>
56. Sawan ME (2012) Damage parameters of structural materials in fusion environment compared to fission reactor irradiation. *Fusion Eng Des* 87:551–555. <https://doi.org/10.1016/j.fusengdes.2012.01.022>
57. Was GS (2016) Fundamentals of radiation materials science: metals and alloys. Springer, Berlin
58. Das S, Armstrong DEJ, Zayachuk Y, Liu W, Xu R, Hofmann F (2018) The effect of helium implantation on the deformation behaviour of tungsten: X-ray micro-diffraction and nanoindentation. *Scr Mater* 146:335–339. <https://doi.org/10.1016/j.scripamat.2017.12.014>
59. Shimada M, Hatano Y, Oya Y, Oda T, Hara M, Cao G, Kobayashi M, Sokolov M, Watanabe H, Tyburska-Püschel B, Ueda Y, Calderoni P, Okuno K (2012) Overview of the US–Japan collaborative investigation on hydrogen isotope retention in neutron-irradiated and ion-damaged tungsten. *Fusion Eng Des* 87:1166–1170. <https://doi.org/10.1016/j.fusengdes.2012.02.103>
60. Yi X, Arakawa K, Ferroni F, Jenkins ML, Han W, Liu P, Wan F (2018) High-temperature damage evolution in 10 keV He+ irradiated W and W-5Re. *Mater Charact* 145:77–86. <https://doi.org/10.1016/j.matchar.2018.08.026>

61. Yi X, Jenkins ML, Kirk MA, Zhou Z, Roberts SG (2016) In-situ TEM studies of 150 keV W + ion irradiated W and W-alloys: damage production and microstructural evolution. *Acta Mater* 112:105–120. <https://doi.org/10.1016/j.actamat.2016.03.051>
62. Ferroni F, Yi X, Arakawa K, Fitzgerald SP, Edmondson PD, Roberts SG (2015) High temperature annealing of ion irradiated tungsten. *Acta Mater* 90:380–393. <https://doi.org/10.1016/j.actamat.2015.01.067>
63. Zhou Z, Jenkins ML, Dudarev SL, Sutton AP, Kirk MA (2006) Simulations of weak-beam diffraction contrast images of dislocation loops by the many-beam Howie–Basinski equations. *Philos Mag* 86:4851–4881. <https://doi.org/10.1080/1478643060615041>
64. Ogorodnikova OV, Dubov LY, Stepanov SV, Terentyev D, Funtkov YV, Shtotsky YV, Stolbunov VS, Efimov V, Gutorov K (2019) Annealing of radiation-induced defects in tungsten: positron annihilation spectroscopy study. *J Nucl Mater* 517:148–151. <https://doi.org/10.1016/j.jnucmat.2019.02.010>
65. Toyama T, Ami K, Inoue K, Nagai Y, Sato K, Xu Q, Hatano Y (2018) Deuterium trapping at vacancy clusters in electron/neutron-irradiated tungsten studied by positron annihilation spectroscopy. *J Nucl Mater* 499:464–470. <https://doi.org/10.1016/j.jnucmat.2017.11.022>
66. Heikinheimo J, Mizohata K, Räisänen J, Ahlgren T, Jalkanen P, Lahtinen A, Catarino N, Alves E, Tuomisto F (2019) Direct observation of mono-vacancy and self-interstitial recovery in tungsten. *APL Mater* 7:21103. <https://doi.org/10.1063/1.5082150>
67. Chung KS, Ice GE (1999) Automated indexing for texture and strain measurement with broad-bandpass x-ray microbeams. *J Appl Phys* 86:5249–5255. <https://doi.org/10.1063/1.1389321>
68. Larson BC, Yang W, Ice GE, Budai JD, Tischler JZ (2002) Three-dimensional X-ray structural microscopy with submicrometre resolution. *Nature* 415:887–890. <https://doi.org/10.1038/415887a>
69. Das S, Liu W, Xu R, Hofmann F (2018) Helium-implantation-induced lattice strains and defects in tungsten probed by X-ray micro-diffraction. *Mater Des* 160:1226–1237. <https://doi.org/10.1016/j.matdes.2018.11.001>
70. Dudarev SL, Mason DR, Tarleton E, Sand AE (2018) Multi-scale model for stresses, strains and swelling of reactor components under irradiation. *Nucl Fusion*. <https://doi.org/10.1088/1741-4326/aadb48>
71. Mason DR, Yi X, Kirk MA, Dudarev SL (2014) Elastic trapping of dislocation loops in cascades in ion-irradiated tungsten foils. *J Phys: Condens Matter* 26:375701. <https://doi.org/10.1088/0953-8984/26/37/375701>
72. Mason DR, Sand AE, Dudarev SL (2019) Atomistic-object kinetic Monte Carlo simulations of irradiation damage in tungsten. *Model Simul Mater Sci Eng* 27:55003. <https://doi.org/10.1088/1361-651x/ab1a1e>
73. Castin N, Bonny G, Bakaev A, Ortiz CJ, Sand AE, Terentyev D (2018) Object kinetic Monte Carlo model for neutron and ion irradiation in tungsten: impact of transmutation and carbon impurities. *J Nucl Mater* 500:15–25. <https://doi.org/10.1016/j.jnucmat.2017.12.014>
74. Troev T, Nankov N, Yoshile T (2014) Simulation of defects in fusion plasma first wall materials. *J Phys: Conf Ser* 516:12022. <https://doi.org/10.1088/1742-6596/516/1/012022>
75. Becquart CS, Domain C (2012) Solute–point defect interactions in bcc systems: focus on first principles modelling in W and RPV steels. *Curr Opin Solid State Mater Sci* 16:115–125. <https://doi.org/10.1016/j.cossms.2012.01.001>
76. Oliver C, Pharr M (1992) An improved technique for determining hardness and elastic modulus using load and displacement sensing indentation experiments. *J Mater Res* 7:1564–1583. <https://doi.org/10.1557/JMR.1992.1564>
77. Armstrong DEJ, Wilkinson AJ, Roberts SG (2011) Mechanical properties of ion-implanted tungsten–5 wt% tantalum. *Phys Scr T145:14076*. <https://doi.org/10.1088/0031-8949/2011/T145/014076>
78. Beck CE, Hofmann F, Eliason JK, Maznev AA, Nelson KA, Armstrong DEJ, Armstrong DEJ (2017) Correcting for contact area changes in nanoindentation using surface acoustic waves. *Scr Mater* 128:83–86. <https://doi.org/10.1016/j.scriptamat.2016.09.037>
79. Gibson J, Armstrong D, Roberts S (2014) The micro-mechanical properties of ion irradiated tungsten. *Phys Scr*. <https://doi.org/10.1088/0031-8949/2014/T159/014056>
80. Armstrong DEJ, Yi X, Marquis EA, Roberts SG (2013) Hardening of self ion implanted tungsten and tungsten 5-wt% rhenium. *J Nucl Mater* 432:428–436. <https://doi.org/10.1016/j.jnucmat.2012.07.044>
81. Hosemann P, Vieh C, Greco RR, Kabra S, Valdez JA, Cappiello MJ, Maloy SA (2009) Nanoindentation on ion irradiated steels. *J Nucl Mater* 389:239–247. <https://doi.org/10.1016/j.jnucmat.2009.02.026>
82. Fleck NA, Hutchinson JW (1997) Strain gradient plasticity. *Adv Appl Mech* 33:295–361. [https://doi.org/10.1016/S0065-2156\(08\)70388-0](https://doi.org/10.1016/S0065-2156(08)70388-0)
83. Britton TB, Hickey JLR (2018) Understanding deformation with high angular resolution electron backscatter diffraction (HR-EBSD). *IOP Conf Ser Mater Sci Eng* 304:12003. <http://stacks.iop.org/1757-899X/304/i=1/a=012003>
84. Das S, Hofmann F, Tarleton E (2018) Consistent determination of geometrically necessary dislocation density from simulations and experiments. *Int J Plast* 109:18–42. <https://doi.org/10.1016/j.ijplas.2018.05.001>
85. Wilkinson AJ (1996) Measurement of elastic strains and small lattice rotations using electron back scatter diffraction. *Ultramicroscopy* 62:237–247. [https://doi.org/10.1016/0304-3991\(95\)00152-2](https://doi.org/10.1016/0304-3991(95)00152-2)
86. Wilkinson AJ, Meaden G, Dingley DJ (2006) High-resolution elastic strain measurement from electron backscatter diffraction patterns: new levels of sensitivity. *Ultramicroscopy* 106:307–313. <https://doi.org/10.1016/j.ultramic.2005.10.001>
87. Liu W, Ice GE, Larson BC, Yang W, Tischler JZ, Budai JD (2004) The three-dimensional X-ray crystal microscope: a new tool for materials characterization. *Metall Mater Trans A* 35:1963–1967. <https://doi.org/10.1007/s11661-004-0145-1>
88. Hofmann F, Abbey B, Liu W, Xu R, Usher BF, Balaur E, Liu Y (2013) X-ray micro-beam characterization of lattice rotations and distortions due to an individual dislocation. *Nat Commun* 4:2774. <https://doi.org/10.1038/ncomms3774>
89. Das S, Yu H, Tarleton E, Hofmann F (2018) Hardening and strain localisation in helium-ion-implanted tungsten, arXiv Prepr. arXiv:1901.00745. <http://arxiv.org/abs/1901.00745>
90. Das S, Yu H, Tarleton E, Hofmann F (2019) Orientation-dependent indentation response of helium-implanted tungsten. *Appl Phys Lett* 114:221905. <https://doi.org/10.1063/1.5097403>
91. Li D, Zbib H, Sun X, Khaleel M (2014) Predicting plastic flow and irradiation hardening of iron single crystal with mechanism-based continuum dislocation dynamics. *Int J Plast* 52:3–17. <https://doi.org/10.1016/j.ijplas.2013.01.015>
92. Lim H, Carroll JD, Battaile CC, Buchheit TE, Boyce BL, Weinberger CR (2014) Grain-scale experimental validation of crystal plasticity finite element simulations of tantalum oligocrystals. *Int J Plast* 60:1–18. <https://doi.org/10.1016/j.ijplas.2014.05.004>
93. Song X, Hofmann F, Korsunsky AM (2010) Dislocation-based plasticity model and micro-beam Laue diffraction analysis of polycrystalline Ni foil: a forward prediction. *Philos Mag* 90:3999–4011. <https://doi.org/10.1080/14786435.2010.502149>

94. Fleck NA, Muller GM, Ashby MF, Hutchinson JW (1994) Strain gradient plasticity: theory and experiment. *Acta Metall Mater* 42:475–487. [https://doi.org/10.1016/0956-7151\(94\)90502-9](https://doi.org/10.1016/0956-7151(94)90502-9)
95. Dunne FPE, Rugg D, Walker A (2007) Lengthscale-dependent, elastically anisotropic, physically-based hcp crystal plasticity: application to cold-dwell fatigue in Ti alloys. *Int J Plast* 23:1061–1083. <https://doi.org/10.1016/j.ijplas.2006.10.013>
96. Roters F (2011) Advanced material models for the crystal plasticity finite element method development of a general CPFEM framework. <http://hdl.handle.net/11858/00-001M-0000-0019-312E-E>
97. Erinosho TO, Dunne FPE (2015) Strain localization and failure in irradiated zircaloy with crystal plasticity. *Int J Plast* 71:170–194. <https://doi.org/10.1016/j.ijplas.2015.05.008>
98. Zhang T, Jiang J, Britton B, Shollock B, Dunne F (2016) Crack nucleation using combined crystal plasticity modelling, high-resolution digital image correlation and high-resolution electron backscatter diffraction in a superalloy containing non-metallic inclusions under fatigue. *Proc R Soc A Math Phys Eng Sci*. <https://doi.org/10.1098/rspa.2015.0792>
99. Zbib HM, Hiratani M, Shehadeh M (2005) Mmultiscale discrete dislocation dynamics plasticity. In: Continuum scale simulation engineering material. Wiley-VCH Verlag GmbH & Co. KGaA, Weinheim, pp 201–229. <https://doi.org/10.1002/3527603786.ch8>
100. Lyu H, Ruimi A, Zbib HM (2015) A dislocation-based model for deformation and size effect in multi-phase steels. *Int J Plast* 72:44–59. <https://doi.org/10.1016/j.ijplas.2015.05.005>
101. Yi X, Sand AE, Mason DR, Kirk MA, Roberts SG, Nordlund K, Dudarev SL (2015) Direct observation of size scaling and elastic interaction between nano-scale defects in collision cascades. *Europhys Lett*. <https://doi.org/10.1209/0295-5075/110/36001>
102. Keys LK, Moteff J (1970) Neutron irradiation and defect recovery of tungsten. *J Nucl Mater* 34:260–280. [https://doi.org/10.1016/0022-3115\(70\)90193-5](https://doi.org/10.1016/0022-3115(70)90193-5)
103. Anand MS, Pande BM, Agarwala RP (1978) Recovery in neutron irradiated tungsten. *Radiat Eff* 39:149–155. <https://doi.org/10.1080/00337577808234468>
104. Kim Y-W, Galligan JM (1978) Radiation damage and stage iii defect annealing in thermal neutron irradiated tungsten. *Acta Metall* 26:379–390. [https://doi.org/10.1016/0001-6160\(78\)90165-7](https://doi.org/10.1016/0001-6160(78)90165-7)
105. Garner FA, Heinisch HL, Simons RL, Mann FM (1990) Implications of neutron spectrum and flux differences on fission-fusion correlations at high neutron fluence. *Radiat Eff Defects Solids* 113:229–255. <https://doi.org/10.1080/10420159008213068>
106. Noda T, Fujita M, Okada M (1998) Transmutation and induced radioactivity of W in the armor and first wall of fusion reactors. *J Nucl Mater* 258–263:934–939. [https://doi.org/10.1016/S0022-3115\(98\)00088-9](https://doi.org/10.1016/S0022-3115(98)00088-9)
107. Iwakiri H, Morishita K, Yoshida N (2002) Effects of helium bombardment on the deuterium behavior in tungsten. *J Nucl Mater* 307–311:135–138. [https://doi.org/10.1016/S0022-3115\(02\)01178-9](https://doi.org/10.1016/S0022-3115(02)01178-9)
108. Roth J, Schmid K (2011) Hydrogen in tungsten as plasma-facing material. *Phys Scr*. <https://doi.org/10.1088/0031-8949/2011/t145/014031>
109. Tanabe T (2014) Review of hydrogen retention in tungsten. *Phys Scr*. <https://doi.org/10.1088/0031-8949/2014/t159/014044>
110. Lindig S, Balden M, Alimov VK, Manhard A, Höschen C, Höschen T, Tyburska-Püschel B, Roth J (2011) Sub-surface structures of {ITER}-grade W (Japan) and re-crystallized W after {ITER}-similar low-energy and high-flux D plasma loadings. *Phys Scr T145:14039*. <https://doi.org/10.1088/0031-8949/2011/t145/014039>
111. Haasz AA, Poon M, Davis JW (1999) The effect of ion damage on deuterium trapping in tungsten. *J Nucl Mater* 266–269:520–525. [https://doi.org/10.1016/S0022-3115\(98\)00586-8](https://doi.org/10.1016/S0022-3115(98)00586-8)
112. Lee HT, Haasz AA, Davis JW, Macaulay-Newcombe RG, Whyte DG, Wright GM (2007) Hydrogen and helium trapping in tungsten under simultaneous irradiations. *J Nucl Mater* 363–365:898–903. <https://doi.org/10.1016/j.jnucmat.2007.01.111>
113. Oya Y, Shimada M, Kobayashi M, Oda T, Hara M, Watanabe H, Hatano Y, Calderoni P, Okuno K (2011) Comparison of deuterium retention for ion-irradiated and neutron-irradiated tungsten. *Phys Scr T145:14050*. <https://doi.org/10.1088/0031-8949/2011/t145/014050>
114. Markelj S, Schwarz-Selinger T, Pečovnik M, Založnik A, Kelemen M, Čadež I, Bauer J, Pelicon P, Chromiński W, Ciupinski L (2019) Displacement damage stabilization by hydrogen presence under simultaneous W ion damage and D ion exposure. *Nucl Fusion* 59:86050. <https://doi.org/10.1088/1741-4326/ab2261>
115. Terentyev D, Bakaeva A, Pardo T, Favache A, Zhurkin EE (2016) Surface hardening induced by high flux plasma in tungsten revealed by nano-indentation. *J Nucl Mater* 476:1–4. <https://doi.org/10.1016/j.jnucmat.2016.04.007>
116. Zayachuk Y, Armstrong DEJ, Bystrov K, Van Boxel S, Morgan T, Roberts SG (2017) Nanoindentation study of the combined effects of crystallography, heat treatment and exposure to high-flux deuterium plasma in tungsten. *J Nucl Mater* 486:183–190. <https://doi.org/10.1016/j.jnucmat.2017.01.026>
117. Hashimoto N, Hunn JD, Parikh N, Gilliam S, Gidcumb S, Patnaik B, Snead LL (2005) Microstructural analysis on helium retention of ion-irradiated and annealed tungsten foils. *J Nucl Mater* 347:307–313. <https://doi.org/10.1016/j.jnucmat.2005.08.010>
118. Yoshida N, Iwakiri H, Tokunaga K, Baba T (2005) Impact of low energy helium irradiation on plasma facing metals. *J Nucl Mater*. <https://doi.org/10.1016/j.jnucmat.2004.10.162>
119. Yang L, Liu H, Zu X (2009) First-principles study of the migration of helium in tungsten. *Int J Mod Phys B* 23:2077–2082. <https://doi.org/10.1142/s0217979209049334>
120. Hammond KD (2017) Helium, hydrogen, and fuzz in plasma-facing materials. *Mater Res Exp*. <https://doi.org/10.1088/2053-1591/aa8c22>
121. Takamura S, Ohno N, Nishijima D, Kajita S (2006) Formation of nanostructured tungsten with arborescent shape due to helium plasma irradiation. *Plasma Fusion Res*. <https://doi.org/10.1585/pfr.1.051>
122. Baldwin MJ, Doerner RP (2008) Helium induced nanoscopic morphology on tungsten under fusion relevant plasma conditions. *Nucl Fusion*. <https://doi.org/10.1088/0029-5515/48/3/035001>
123. Nishijima D, Ye MY, Ohno N, Takamura S (2004) Formation mechanism of bubbles and holes on tungsten surface with low-energy and high-flux helium plasma irradiation in NAGDIS-II. *J Nucl Mater* 329–333:1029–1033. <https://doi.org/10.1016/j.jnucmat.2004.04.129>
124. Tokunaga K, Tamura S, Yoshida N, Ezato K, Taniguchi M, Sato K, Suzuki S, Akiba M (2004) Synergistic effects of high heat loading and helium irradiation of tungsten. *J Nucl Mater* 329–333:757–760. <https://doi.org/10.1016/j.jnucmat.2004.04.178>
125. Cipiti BB, Kulcinski GL (2005) Helium and deuterium implantation in tungsten at elevated temperatures. *J Nucl Mater* 347:298–306. <https://doi.org/10.1016/j.jnucmat.2005.08.009>
126. Zenobia SJ, Garrison LM, Kulcinski GL (2012) The response of polycrystalline tungsten to 30 keV helium ion implantation at normal incidence and high temperatures. *J Nucl Mater* 425:83–92. <https://doi.org/10.1016/j.jnucmat.2011.10.029>
127. Boisse J, Domain C, Becquart CS (2014) Modelling self trapping and trap mutation in tungsten using DFT and molecular dynamics with an empirical potential based on DFT.

- J Nucl Mater 455:10–15. <https://doi.org/10.1016/j.jnucmat.2014.02.031>
128. Becquart CS, Barthe MF, De Backer A (2011) Modelling radiation damage and He production in tungsten. Phys Scr T145:14048. <https://doi.org/10.1088/0031-8949/2011/T145/014048>
129. Armstrong DEJ, Edmondson PD, Roberts SG (2013) Effects of sequential tungsten and helium ion implantation on nano-indentation hardness of tungsten. Appl Phys Lett 251901:1–5. <https://doi.org/10.1063/1.4811825>
130. Hofmann F, Mason DR, Eliason JK, Maznev AA, Nelson KA, Dudarev SL (2015) Non-contact measurement of thermal diffusivity in ion-implanted nuclear materials. Sci Rep 5:16042. <https://doi.org/10.1038/srep16042>
131. Makin MJ, Sharp JV (1965) A model of lattice hardening in irradiated copper crystals with the external characteristics of source hardening. Phys Status Solidi 9:109–118. <https://doi.org/10.1002/pssb.19650090114>
132. Sharp J (1974) Deformation of neutron irradiated copper alloys. Acta Metall 22:449
133. Hashimoto N, Byun TS, Farrell K, Zinkle SJ (2005) Deformation microstructure of neutron-irradiated pure polycrystalline vanadium. J Nucl Mater 336:225–232. <https://doi.org/10.1016/j.jnucmat.2004.09.017>
134. Kacher J, Liu G, Robertson I (2012) In situ and tomographic observations of defect free channel formation in ion irradiated stainless steels. Micron 43:1099–1107. <https://doi.org/10.1016/j.micron.2012.01.017>
135. Tulluri R, Morrison DJ (1997) Effects of ion irradiation on fatigue of Fe-12Cr-20Mn stainless steel for fusion reactor applications. J Mater Eng Perform 6:454–460. <https://doi.org/10.1007/s11665-997-0116-y>
136. Zinkle SJ, Singh BN (2006) Microstructure of neutron-irradiated iron before and after tensile deformation. J Nucl Mater 351:269–284. <https://doi.org/10.1016/j.jnucmat.2006.02.031>
137. Ren C, Fang ZZ, Xu L, Ligda JP, Paramore JD, Butler BG (2019) An investigation of the microstructure and ductility of annealed cold-rolled tungsten. Acta Mater 162:202–213. <https://doi.org/10.1016/j.actamat.2018.10.002>
138. Guo W, Cheng L, De Temmerman G, Yuan Y, Lu GH (2018) Retarded recrystallization of helium-exposed tungsten. Nucl Fusion. <https://doi.org/10.1088/1741-4326/aad2b0>
139. Knaster J, Moeslang A, Muroga T (2016) Materials research for fusion. Nat Phys 12:424–434. <https://doi.org/10.1038/NPHYS3735>
140. Armstrong DEJ, Hardie CD, Gibson JSKL, Bushby AJ, Edmondson PD, Roberts SG (2015) Small-scale characterisation of irradiated nuclear materials: part II nanoindentation and micro-cantilever testing of ion irradiated nuclear materials. J Nucl Mater 462:374–381. <https://doi.org/10.1016/j.jnucmat.2015.01.053>

**Publisher's Note** Springer Nature remains neutral with regard to jurisdictional claims in published maps and institutional affiliations.